Lithospheric architecture and tectonic evolution of the southwestern U.S. Cordillera: constraints from zircon Hf and O isotopic data

*Chapman, J.B.[1]

Dafov, M.N.[1]

Gehrels, G.[1]

Ducea. M.N.[1, 2]

Valley, J.W.[3]

Ishida, A.[3, 4]

*Corresponding author

[1]Department of Geosciences, University of Arizona, Tucson, Arizona 85721

[2]Faculty of Geology and Geophysics, University of Bucharest, 010041, Bucharest, Romania

[3]Department of Geoscience, University of Wisconsin, Madison, Wisconsin 53706

[4]Institute for Excellence in Higher Education, Tohoku University, Sendai 9808576, Japan

Abstract

Radiogenic and stable isotopic studies of zircon are a powerful tool to investigate geologic processes because data can be placed in a temporal context using U-Pb ages. However, when zircon data lack information on the spatial distribution of the parent rock(s) (e.g., detrital datasets), interpreting changes in isotopic composition through time is not always straightforward. To evaluate and improve the utility of zircon isotopic data, we present a regional dataset consisting of new zircon U-Pb, $\varepsilon Hf_{(t)}$ and $\delta^{18}O_{zrc}$ data in 31 Triassic to early Miocene igneous rocks from a >1,300 km long transect in the southwestern U.S. Cordillera. This dataset is combined and compared with a compilation of whole rock isotopic data from the same transect. Orogen-scale spatial and temporal isotopic trends are identified and interpreted, both in terms of the underlying mechanisms that generated the trends and the tectonic

processes that have shaped this part of the Cordillera. Most Cordilleran magmatism originates in the upper mantle and zircon $\varepsilon Hf_{(t)}$ primarily reflects the isotopic composition of the mantle source region. East of ~114 °W longitude in the southwestern U.S. Cordillera, the continental mantle lithosphere remained coupled to the crust until the late Miocene and zircon $\varepsilon Hf_{(t)}$ reflects the age of the lithosphere. Because the mantle lithosphere remained intact, zircon $\varepsilon Hf_{(t)}$ and $\delta^{18}O_{zrc}$ of igneous rocks associated with low-angle to flat-slab subduction and crustal thickening during the Laramide orogeny are not significantly different from igneous rocks associated with Farallon slab rollback/foundering. Temporal isotopic trends identified in rocks east of ~114 °W longitude are related to migration of magmatism into lithospheric terranes of different age. West of ~114 °E longitude, in regions like the Mojave Desert in southern California, the continental mantle lithosphere is interpreted to have been partially removed and replaced by underplated Pelona-Orocopia-Rand schist and isotopically depleted asthenosphere or oceanic lithosphere during the Laramide orogeny. There is a temporal isotopic shift to more juvenile zircon $\varepsilon Hf_{(t)}$ and higher $\delta^{18}O_{zrc}$ in igneous rocks west of ~114 °W, which is used to estimate the position of the western edge of intact North American continental mantle lithosphere before and after the Laramide orogeny. The results suggest that regional (spatial) trends in zircon $\varepsilon Hf_{(t)}$ and $\delta^{18}O_{zrc}$ data can be significantly larger than isotopic shifts at a specific location within a Cordilleran orogenic system. By accounting for regional spatial variations, temporal isotopic trends in zircon data can be more confidently interpreted in terms of tectonic and geodynamics processes.

1. Introduction

A defining characteristic of Cordilleran orogenic systems is a rich record of subduction-related magmatism, which provides insight into lithospheric architecture as well as tectonic and geodynamic processes (Ducea et al., 2015). Continental subduction systems and Cordilleran orogens cycle (10s Myr) between extensional and contractional end-members, a fundamental feature in models for orogenic cyclity (DeCelles et al., 2009; 2015; Ramos, 2009; Wells et al., 2012). The radiogenic isotopic composition of continental arc magmatism is a key tool used to track these cycles (Ducea, 2001; Haschke et al., 2002;

Ducea and Barton, 2007). Kemp et al. (2009) demonstrated that zircon Lu-Hf and zircon O isotope ratios in igneous rocks can help distinguish contractional and extensional periods such as: slab roll-back, back-arc basin extension, basin closure, and lithospheric thickening. Zircon Lu-Hf isotopic data, including detrital zircon data, have recently been examined in numerous orogens to understand these processes and to help interpret periods of contraction and extension in the geologic record (Zhu et al., 2011; Boekhout et al., 2015; Balgord, 2017). However, a recent review of Cordilleran orogenic magmatism by Chapman et al. (2017) suggests that the isotopic composition of the continental lithosphere and, in particular, the presence or absence of the mantle lithosphere may exert a primary control on the zircon Lu-Hf isotopic composition of magmatic products. In this view, temporal shifts in the isotopic composition of magmatism in Cordilleran orogens are commonly related to the migration of magmatism into different lithospheric provinces or into regions with more or less continental mantle lithosphere preserved.

The southwestern U.S. Cordillera has experienced multiple episodes of extension, contraction, and arc migration during the Mesozoic to Cenozoic and the magmatic record is nearly continuous during this time (DeCelles, 2004; Dickinson, 2004; DeCelles and Graham, 2015). The impetus for this study was to test if the zircon Lu-Hf and zircon O isotopic composition of Mesozoic to early Miocene igneous rocks from the southwestern U.S. Cordillera reflect geodynamic changes. The results presented constitute the first regional zircon Lu-Hf and zircon O isotopic dataset from Mesozoic and younger igneous rocks in this part of the U.S. Cordillera (Fig. 1; Table 1).

2. Geologic Background: Southwestern U.S. Cordillera

The U.S. Cordillera evolved since Paleozoic time as a result of subduction of oceanic lithosphere beneath the western North American plate (Dickinson, 2004). Widespread subduction beneath North America initiated during the Triassic and lasted until the subduction of the Pacific-Farallon mid-oceanic spreading center and development of the San Andreas transform plate boundary during the late Oligocene to Miocene (Atwater and Stock, 1998). Opening of the north Atlantic Ocean during the Middle Jurassic coincided with an increase in North America-Farallon convergence rate and may have been linked to the

start of contractional deformation in the Sevier retroarc thrust belt in the central U.S. Cordillera (DeCelles, 2004). In contrast to the central U.S. Cordillera, during the Jurassic, much of the southwestern U.S. Cordillera was marked by extension and the development of the Bisbee-Sabinas rift basin that has been linked to the opening of the Gulf of Mexico (Dickinson and Lawton, 2001a) and back-arc to intra-arc transtension (DeCelles, 2004; Busby, 2012). Subduction rollback of the Farallon plate facilitated this extension and led to rifting of the Guerrero terrane and opening of the Arperos Basin (Lawton and McMillan, 1999; Martini et al., 2014) (Fig. 2A). Regional extension and rifting might be expected to shift Lu-Hf isotope ratios in continental arc rocks to more juvenile compositions (cf., Boekhout et al., 2015). Rifting and post-extension thermal subsidence lasted until the mid-Cretaceous (~100 Ma) at which time the Arperos Basin closed and the region transitioned into a contractional environment (Dickinson and Lawton, 2001a; Spencer et al., 2011; Martini et al., 2014). Despite widespread extensional deformation during the Jurassic, regionally significant shortening also occurred in the East Sierran Thrust System (Dunne and Walker, 2004).

From the mid-Cretaceous to the start of the Laramide orogeny (~80 Ma), foreland basin deposits (Barth et al., 2004; Spencer et al., 2011; Clinkscales and Lawton, 2015) and shortening in the Maria fold-thrust belt (Spencer and Reynolds, 1990) and Mexican fold-thrust belt (Fitz-Diaz et al., 2017) suggest that the southwestern U.S. Cordillera was part of a retroarc thrust belt and retroarc foreland basin system (Fig. 2B). Prior to the Laramide orogeny, oceanic subduction is recorded by calc-alkaline, intermediate (andesitic), sublinear volcanic arcs and batholiths (Dickinson, 2004). The southwestern U.S. Cordilleran subduction system initiated during the Late Permian (Walker, 1988) and produced voluminous (high-flux) magmatic events during the 1) Triassic (Riggs et al., 2013), 2) the Late Jurassic (Barth et al., 2017), and 3) the mid- to Late-Cretaceous that comprises the bulk of the Sierra Nevada and Peninsular Ranges batholiths (Cecil et al., 2012).

The Laramide orogeny (80-40 Ma) is thought to be related to low-angle or flat-slab subduction of the Farallon plate (Fig. 2C), associated with subduction of an oceanic plateau (Coney and Reynolds, 1977; Saleeby, 2003; Liu et al., 2010). Continental arc magmatism in the Sierra Nevada and Peninsular Ranges batholiths ended by ~80 Ma (Ducea, 2001) and magmatism migrated eastward toward the

106 foreland, reaching its maximum eastern extent in the Big Bend region of Texas and Sierra Madre Oriental
107 in Mexico during the Late Eocene (Constenius et al., 2003; Fitz-Díaz et al., 2017). Most Laramide-age
108 magmatism is calc-alkaline, metaluminous, and associated with subduction processes (Lang and Titley,
109 1998; McMillan, 2004). A broad belt of Laramide-age peraluminous (S-type) granite is also present in
110 the Cordillera and has been attributed to crustal anatexis (Miller and Barton, 1990). Crustal melting may
111 have been driven by asthenospheric upwelling following delamination (Wells et al., 2012) or by
112 radiogenic heating associated with crustal thickening (Farmer and DePaolo, 1984). The Laramide
113 orogeny in the southwestern U.S. Cordillera is associated with basement-involved, high-angle reverse
114 faulting, block uplifts, and localized basin sedimentation associated with these uplifts (Davis, 1979;
115 Dickinson et al., 1988; Clinkscales and Lawton, 2015) (Fig. 2C). Crustal thickening and contraction
116 associated with the Laramide orogeny might be expected to shift Lu-Hf isotope ratios in magmatic rocks
117 to more evolved compositions (cf., Boekhout et al., 2015). Isolated exposures of the Late Cretaceous to
118 Eocene Pelona-Orocopia-Rand schist are present in the southwestern U.S. Cordillera west of ~113.5 °W
119 longitude and are inferred to be the result of subduction erosion and underplating of the accretionary
120 complex and forearc during the Laramide orogeny (Grove et al., 2003; Ducea et al., 2009; Chapman,
121 2017 and references therein).
122 The end of the Laramide orogeny in the southwestern U.S. Cordillera is marked by a transition
123 from contractional to extensional tectonics around 40 Ma (Constenius et al., 2003) (Fig. 3). The
124 transition to extension is generally attributed to rollback and foundering of the Farallon slab, which has
125 also been associated with a rapid westward sweep of magmatism toward the plate margin (Fig. 2d)
126 (Coney and Reynolds, 1977; Humphreys, 1995). This magmatic event lasted in the Cordilleran interior
127 until the middle Miocene, was widespread, voluminous, and includes the "ignimbrite flare-up" of western
128 North America with a peak in activity between 25-30 Ma (Lipman, 1992). During the Oligocene to early
129 Miocene, extension initiated in the Rio Grande rift (Ricketts et al., 2016) and large-magnitude slip on
130 low-angle normal fault systems helped to exhume a series of metamorphic core complexes in the
131 Colorado River extensional corridor, southern Arizona, Sonora, and the eastern Mojave region
132 (Dickinson, 1991) (Fig. 2d). Dickinson (1991) referred to this stage (~30-15 Ma) of extension, dominated

by low-angle normal faulting, as the mid-Tertiary taphrogeny and distinguished it from subsequent "Basin and Range" extension within the southwestern U.S. Cordillera. Lithospheric extension and extension during this time might be expected to shift Lu-Hf isotope ratios in magmatic rocks to more juvenile compositions (cf., Boekhout et al., 2015).

Basin and Range style extension is most prominent in the central part of southwestern U.S. Cordillera (Arizona, New Mexico) and is characterized by high-angle normal faults and the formation of ~north-south trending half-graben systems (Dickinson, 1991; Spencer et al., 1995). The majority of Basin and Range style extension occurred between the middle Miocene and Pliocene (McQuarrie and Wernicke, 2005). Starting in the Miocene, there was a pronounced shift in the composition of magmatism in the U.S. Cordillera. Intermediate to felsic ignimbrite-related magmatism was replaced by bimodal, predominantly basaltic, magmatism (Armstrong and Ward, 1991). This shift is closely linked to Basin and Range extension and as extension progressed from the late Miocene to the present, magmatism in the southwestern U.S. Cordillera became increasingly characterized by the eruption of tholeiitic and alkali basalt with asthenospheric major and trace element patterns and juvenile isotopic compositions (e.g., Wang et al., 2002). The start of Basin and Range extension is interpreted to mark the end of the Cordilleran-style orogenic processes and magmatism < 15 Ma is not considered in this study.

2.1. Lower crustal structure and basement terranes, southwestern U.S. Cordillera

The central U.S. Cordillera contains terranes of possible allochthonous origin (e.g., Roberts Mountains allochthon) that were accreted to the North American plate in the Paleozoic (e.g., Antler orogeny; Speed and Sleep, 1982; Dickinson, 2004). Several isotopic studies on magmatic rocks have helped to delineate the boundary between these terranes and North American basement rocks (King et al., 2004; and references therein); however, the boundary is most commonly associated with the $^{87}Sr/^{86}Sr$ = 0.706 isopleth, colloquially called the "706 line" (Kistler and Peterman, 1973) (Fig. 1). More radiogenic (evolved) isotopic values in Mesozoic and Cenozoic igneous rocks occur east of the 706 line. In the southwestern U.S. Cordillera, the 706 line parallels the crest of the southern Sierra Nevada and is

truncated against the Garlock fault (Kistler, 1990) (Fig. 1). The 706 line in the southern Sierra Nevada has been interpreted to mark the edge of continental basement (Kistler, 1990) as well as the edge of North American mantle lithosphere (Coleman and Glazner, 1997). Mantle xenoliths from the eastern Sierra Nevada indicate that the base of the mantle lithosphere was located at >100 km depth during the Mesozoic and that the radiogenic isotopic compositions of Mesozoic plutons in the eastern Sierra Nevada are similar to the isotopic composition of the Mesozoic mantle lithosphere (Ducea and Saleeby, 1998; Ducea, 2001).

The southwestern U.S. Cordillera does not contain any large accreted terranes like the central and northern U.S. Cordillera. There are a few ranges in the northwest Mojave Desert region (e.g., El Paso Mountains) containing basement rocks correlated with the Roberts Mountains allochthon that have been displaced southward by sinistral strike slip and then thrust over North American lithosphere (Miller et al., 1995), but samples from this study did not come from these locations. North American crystalline basement is thought to extend westward across the Mojave region to the San Andreas Fault (Martin and Walker, 1992) and the thickest section of the North American Proterozoic to Paleozoic passive margin sequence (Cordilleran miogeocline) occurs in the western Mojave region (Stewart, 2005).

The Proterozoic continental lithosphere in the southwestern U.S. Cordillera consists of several tectonostratigraphic terranes or provinces including, from oldest to youngest, the Mojave, Yavapai, Mazatzal, and Grenville terranes (Whitmeyer and Karlstrom, 2007) (Fig. 1). The Mojave crustal province records Paleoproterozoic continental crust formation, incorporates rocks as old as the Archean, and has a mean crustal Sm-Nd model age of ~2.2 Ga (Wooden et al., 2013). Formation and accretion of juvenile crust occurred in the Yavapai province at 1.7-1.8 Ga, the Mazatzal province at 1.6-1.7 Ga, and the Grenville province at 1.0-1.3 Ga (Whitmeyer and Karlstrom, 2007, and references therein). The Nd isotopic composition of Mesozoic and younger magmatic rocks has been used to define isotopic provinces, which roughly mimic the geographic position of Proterozoic terranes based on U-Pb studies (Bennett and DePaolo, 1987).

3. Analytical methods

Rock samples were processed at the University of Arizona using standard methods for isolating zircon including magnetic and heavy liquid separation techniques. Zircon crystals from the same sample were used for U-Pb geochronology, Lu-Hf isotope geochemistry, and O isotope geochemistry. Zircon crystals were mounted in epoxy along with relevant standards and then polished to expose a cross-section of the crystal interior. Epoxy mounts were imaged by backscatter electron (BSE) and cathodoluminescence (CL) detectors on a Hitachi 3400N scanning electron microscope (SEM) at the Arizona LaserChron SEM facility. Locations for zircon U-Pb, Lu-Hf, and O isotopic analyses were chosen using a combination of high-resolution BSE and CL images.

U-Th-Pb isotope ratios were collected at the University of Arizona Laserchon Center (www.laserchon.org) using a Teledyne Photon Machines G2™ solid state NeF excimer laser ablation system coupled to a Thermo Fisher Scientific ELEMENT 2™ single collector inductively coupled plasma mass spectrometer (LA-ICP-MS). Data were collected and reduced following the procedures described by Gehrels et al. (2008) and Gehrels and Pecha (2014). The value, uncertainty, and scatter of the zircon standards during the analytical sessions was 1098.7 ± 0.7 Ma for the primary standard FC-1 (range = 1004-1199 Ma), 557.0 ± 0.4 Ma for the secondary standard SL (range = 532-587 Ma), and 418.2 ± 0.4 Ma for the secondary standard R33 (range = 399-439 Ma). All analyses with acceptable precision, discordance, and in-run fractionation are presented in Supplementary Table 1. Acceptable discordance (comparing $^{206}Pb/^{238}U$ and $^{206}Pb/^{207}Pb$ ages) is < 20% and < 5% for reverse discordance. Discordance filters are only applied to ages > 400 Ma. The reported U-Pb age for each sample is a weighted mean of 5-23 individual zircon U-Pb analyses. Because all samples have Mesozoic or younger crystallization ages, $^{206}Pb/^{238}U$ ratios were used to calculate weighted mean ages. Uncertainty is reported at the 2σ level and includes internal and external uncertainties added in quadrature (Table 1).

Zircon Lu-Hf isotope geochemistry was conducted by LA-ICP-MS at the Arizona LaserChron Center using a Nu Instruments multi-collector mass spectrometer coupled to a Teledyne Photon Machines G2™ laser system. Measurements were made using a 40 μm diameter spot placed directly over a

previous 20 μm U-Pb ablation pit. Data collection and reduction follows the procedures described in Cecil et al. (2011) and Gehrels and Pecha (2014). After adjusting mass bias to reduce offset, the value, uncertainty, and scatter of the zircon standards during the analytical sessions was 0.28218 ± 0.00005 $^{176}Hf/^{177}Hf$ for FC-52 (range = 0.28208 - 0.28269 $^{176}Hf/^{177}Hf$), 0.28267± 0.00003 $^{176}Hf/^{177}Hf$ for Temora-2 (range = 0.28259 - 0.28274 $^{176}Hf/^{177}Hf$), 0.28254 ± 0.00003 $^{176}Hf/^{177}Hf$ for Mud Tank (range = 0.28247 - 0.28259 $^{176}Hf/^{177}Hf$), 0.28250 ± 0.00004 $^{176}Hf/^{177}Hf$ for Plesovice (range = 0.28245 - 0.28277 $^{176}Hf/^{177}Hf$), 0.28275 ± 0.00003 $^{176}Hf/^{177}Hf$ for R33 (range = 0.28266 - 0.28288 $^{176}Hf/^{177}Hf$), and 0.28232 ± 0.00005 $^{176}Hf/^{177}Hf$ for 91500 (range = 0.28219 - 0.28275 $^{176}Hf/^{177}Hf$). Lu-Hf isotopic data are presented throughout the paper using epsilon notation, in which $^{176}Hf/^{177}Hf$ ratios are expressed relative to the chondritic uniform reservoir (CHUR; Bouvier et al., 2008). $\varepsilon Hf_{(t)}$ refers to the εHf isotopic composition at the time of zircon crystallization. Results and internal precision for $^{176}Hf/^{177}Hf$ and εHf are reported for each analysis in Supplemental Table 2. Reported $\varepsilon Hf_{(t)}$ values are weighted means of 5-15 individual zircon $\varepsilon Hf_{(t)}$ analyses and 2σ uncertainties are reported by combining external and internal uncertainty in quadrature. Single zircon $\varepsilon Hf_{(t)}$ analysis values were excluded from mean sample values when the corresponding single-grain zircon U-Pb analysis indicated the spot was part of an inherited age domain (generally >3σ larger than the youngest age population; Supplementary Table 2).

Zircon oxygen isotope ratios were measured by secondary ion mass spectroscopy (SIMS) at the WiscSIMS laboratory at the University of Wisconsin-Madison using a CAMECA IMS 1280 ion microprobe using procedures described elsewhere (Kita et al., 2009; Valley and Kita, 2009 and references therein). Sample zircon grains were mounted in epoxy resin with the running reference material, KIM-5 zircon (Valley, 2003), and coated by gold. The primary Cs+ beam with intensity of ~1.6 nA, was focused to an analysis spot size of ~12 μm on a polished zircon surface (separate mounts from U-Pb Lu-Hf analyses). CL images of zircons from samples previously analyzed for U-Pb isotopes were used to guide analysis locations, although inadvertent analyses of multiple zircon age domains may have occurred. Secondary ions of $^{16}O^-$ and $^{18}O^-$ were detected by two Faraday Cup detectors for oxygen two isotope analysis and $^{16}OH^-$ was detected by electron multiplier to monitor the influence of contaminant, simultaneously. For zircons, elevated OH/O ratios, when corrected for background, are typical for

238 domains with high degree of radiation damage (Wang et al., 2014). A single analysis took 3 minutes,
239 which includes an initial pre-sputtering (10s), automatic centering of secondary ions (~60s), and
240 integration of oxygen isotope signals (4s × 20 cycle). Oxygen isotopic data is reported in per mil (‰)
241 using delta notation relative to Vienna standard mean ocean water (VSMOW). Instrumental mass bias of
242 oxygen isotope ratio was calibrated by bracketing analysis of KIM-5 zircon for every ~10 unknown
243 analyses, typically four analyses at the start of each bracket and four at the end. Average mass bias of the
244 entire session was -2.02 ‰ (range = -1.75 to -2.32). Based on in-run analysis of KIM-5 zircon, the
245 average precision of $\delta^{18}O_{zrc}$ is ≤ 0.3‰ (2 standard error [SE]). Reported $\delta^{18}O_{zrc}$ in Table 1 is a weighted
246 mean of 7-13 individual zircon $\delta^{18}O$ analyses using 2 SE external precision as the weighting factor. The
247 uncertainty of $\delta^{18}O_{zrc}$ values reported in Table 1 represents intra-sample variation and is reported as two
248 standard deviations of the range of values from each sample. Complete results for unknown and standard
249 analyses are presented in Supplementary Table 3.
250 In addition to new analyses, existing εNd and $\delta^{18}O$ data were compiled from the North American
251 Volcanic and Intrusive Rock Database (NADAT; navdat.org). The compiled data comes from the same
252 geographic range as the transect samples and excludes samples < 15 Ma, which are often characterized by
253 juvenile isotopic compositions related to Basin and Range extension. A table of all compiled data and
254 data sources is presented in Supplementary Table 4. Compiled $\delta^{18}O$ data comes from intrusive and
255 extrusive whole rock samples and mineral analyses other than zircon. For comparison purposes,
256 equilibrium fractionation ($\Delta^{18}O$) between whole rock and zircon analyses is estimated using the
257 calibration from Lackey et al. (2008) that incorporates whole rock SiO_2 contents. Equilibrium
258 fractionation at magmatic temperatures for other mineral-zircon pairs used to compare data in this study
259 are; $\Delta^{18}O_{quartz\text{-}zrc} = 2.2$; $\Delta^{18}O_{sanidine\text{-}zrc} = 1.45$; $\Delta^{18}O_{plagioclase\text{-}zrc} = 1.0$ (Bindeman and Valley, 2001; Valley et
260 al., 2003; Trail et al., 2009). For comparison purposes, whole rock $\varepsilon Nd_{(t)}$ is related to zircon $\varepsilon Hf_{(t)}$ using
261 the terrestrial array of Vervoort et al. (1999). Beard and Johnson (1997) There is minor isotopic
262 fractionation between zircon Hf analyses and the parent whole rock Hf analyses (Kinny and Maas, 2003),
263 which allows the comparison of whole rock $\varepsilon Nd_{(t)}$ to zircon $\varepsilon Hf_{(t)}$. Converted εNd and $\delta^{18}O$ data are
264 included in Supplementary Table 4.

4. Results

Zircon was analyzed from 31 samples of igneous rocks (mainly intrusive) collected from an ~1,300 km long transect across the southwestern U.S. Cordillera, from the southern Sierra Nevada in California to west Texas (~118.5 °W to ~105.5 °W longitude and ~31.75 °N to ~35.25 °N latitude) (Fig. 1; Table 1). This study reports new zircon U-Pb ages for 25 samples, 30 new zircon Lu-Hf isotopic ranges, and 20 new zircon oxygen isotopic ranges (Table 1). Basic descriptions of each sample and detailed zircon U-Pb, zircon Lu-Hf, and zircon $\delta^{18}O$ results for each sample are provided in Supplementary File 1. Samples were chosen based on geographic distribution (from a range of longitudes) and age (Mesozoic to early Miocene) to explore temporal and spatial isotopic changes (Figs. 2-3). Samples <15 Ma were avoided, as many igneous rocks of this age in the southwestern U.S. are associated with Basin and Range extension and their isotopic composition may not reflect Cordilleran (continental arc) tectonic processes. Igneous rock classification in Table 1 is based on appearance in the field or, when available, from chemical analyses published in previous studies (Supplemental File 1). Individual samples were not analyzed chemically in this study and are not intended to be representative of the entire compositional range of a pluton or intrusive suite.

4.1. Zircon U-Pb geochronology results

Results of zircon U-Pb geochronology are presented in Table 1. To our knowledge, all the ages presented are broadly consistent with previous studies. References to previous studies for individual plutons or igneous suites are provided for each sample in Supplementary File 1. All weighted mean zircon U-Pb ages presented in Table 1 are interpreted as crystallization/emplacement ages and exclude old ages obtained from premagmatic zircon cores and occasionally young ages interpreted to be related to loss of radiogenic Pb (Supplementary Table 1; Supplementary File 1). Average U/Th of zircon analyses used to calculate crystallization ages are < 5 for all samples (Supplemental Table 1). Five of the samples (Tyrone, San Juan, Chino, Ajo, and Lakeshore) were previously dated by Leveille and Stegen (2012)

using zircon U-Pb isotope geochronology. The age of sample 29-Palms was adopted from zircon U-Pb isotopic data presented in Barth and Wooden (2006). Late Cretaceous and younger igneous rocks in this study show the same spatial-temporal patterns (eastward migration followed by westward migration; Fig. 3) documented in previous compilations of igneous rock ages from the U.S. Cordillera (Coney and Reynolds, 1977; Constenius et al., 2003).

Pre-magmatic and/or xenocrystic cores were analyzed for U-Pb when encountered (based on CL images), but not investigated systematically. Premagmatic (inherited) zircon cores range in age from Mesozoic to Proterozoic (Supplemental Table 1). Inherited (single-grain) ages are shown in Fig. 5 where analyses are grouped by the crustal province the parent sample was collected from (Fig. 1). Although it is not a comprehensive dataset, the Proterozoic inherited zircon ages are broadly consistent with published ranges of basement ages for the crustal provinces (Whitmeyer and Karlstrom, 2007), excluding inherited zircon ages from the Mojave province (sample size n=11) and Yavapai province (n=3), which are younger than expected.

4.2. Zircon Lu-Hf isotope results

Results of zircon Lu-Hf isotopic analyses are presented in Table 1, Figs. 3-6, and Supplementary Table 2. Reported weighted mean zircon $\varepsilon Hf_{(t)}$ values are calculated from zircon grains that have U-Pb ages consistent with the crystallization/emplacement age. Most samples have uncertainties of < 2 εHf units for mean values (Table 1), although uncertainty is high (up to 6 εHf units) for some samples.

Zircon $\varepsilon Hf_{(t)}$ data show little or no secular trend but significant regional distinctions. Plotting isotopic data from the southwestern U.S. Cordillera against sample age, as is commonly done for detrital zircon $\varepsilon Hf_{(t)}$ data (e.g., Gehrels and Pecha, 2014), revealed a possible trend of increasing $\varepsilon Hf_{(t)}$ from the Late Cretaceous to the early Miocene (Fig. 4a), although no clear trends are easily recognizable. A compilation of $\varepsilon Nd_{(t)}$ data from the southern U.S. Cordillera (Supplementary Table 4) also shows a large range of isotopic values at many points in time without a clear temporal trend (Fig. 4b).

316 Regional isotopic trends are most apparent when plotted against longitude (Fig. 6), which is sub-
317 parallel to the structural grain of the Cordillera. Zircon $\varepsilon Hf_{(t)}$ data in Fig. 6a form a broad U-shaped
318 pattern with the most isotopically juvenile values (+10 to +15 $\varepsilon Hf_{(t)}$) in the western Mojave Desert and
319 Sierra Nevada, the most isotopically evolved values (-10 to -15 $\varepsilon Hf_{(t)}$) around ~114 °W longitude, and
320 relatively juvenile values (0 to +10 $\varepsilon Hf_{(t)}$) in west Texas. The spatial change (ε/distance) in isotopic
321 values is greatest (steepest) in the west. Compiled $\varepsilon Nd_{(t)}$ data in Fig. 6a corroborate this trend.
322 Data in Fig. 6a are separated into samples older and younger than 40 Ma, the approximate end of
323 the Laramide orogeny and the initial age of a switch from a contractional to extensional tectonic regime in
324 the southwestern U.S. Cordillera (Fig. 3; Constenius et al., 2003). The "> 40 Ma" and "< 40 Ma" bands
325 in Fig. 6a encompass all of the new Hf isotopic data and ~90% of the compiled Nd isotopic data. At any
326 longitudinal position in the southwestern U.S. Cordillera there is variation in the isotopic composition of
327 magmatic rocks, but most of these values fall within a ~10 epsilon unit range, outlined by dashed lines or
328 "bands" in Figure 6a. In samples older than 40 Ma, the lowest $\varepsilon Hf_{(t)}$ and $\varepsilon Nd_{(t)}$ values occur at 117 °W to
329 116 °W longitude. Both $\varepsilon Hf_{(t)}$ and $\varepsilon Nd_{(t)}$ samples younger than 40 Ma exhibit a shift to more juvenile
330 radiogenic isotopic compositions west of ~114 °W longitude, but no shift in composition east of ~114 °W
331 longitude (Fig. 6a). Hf isotopic compositions of samples < 40 Ma are most negative at 109 °W to 111 °W
332 longitude and Nd isotopic compositions of samples < 40 Ma are most negative at 112 °W to 115 °W
333 longitude.
334 Nd and Hf isotopic composition can vary with whole rock composition. No chemical data were
335 collected for the new samples in this study, but when compiled Nd isotopic data are plotted by whole rock
336 SiO_2 content (Fig. 7b), the most mafic samples tend to have the highest values within a ~10 epsilon unit
337 range, which is similar to the magnitude (y-axis range) of the "< 40 Ma" and "> 40 Ma" bands in Fig. 6a.
338 The total longitudinal (spatial) isotopic range in Figs. 6a and 7b is larger (~30 epsilon units) than the ~10
339 epsilon unit isotopic range at any single longitude associated with changes in rock composition.
340 In addition to mean $\varepsilon Hf_{(t)}$ values corresponding to rock crystallization age, single-grain Lu-Hf
341 isotopic analyses of inherited zircon age domains were obtained on domains identified during previous U-
342 Pb analyses (Supplemental Table 2). Zircon $\varepsilon Hf_{(t)}$ results for samples with Proterozoic ages from

inherited cores are plotted in Fig. 5 and grouped by crustal province. The dataset is not comprehensive, but zircon grains from the same province generally fall along similar $^{176}Lu/^{177}Hf = 0.015$ crustal evolution lines, excluding the Mojave province. Some analyses from the Mojave province appear to have either evolved from a more compatible (higher Lu/Hf) source (i.e., shallower slope of an evolution line in ε-space) or to have experienced significant isotopic mixing with a more juvenile component during Phanerozoic crystallization. Hf model ages, based on the crustal evolution lines in Fig. 5, for samples in the Grenville and Mazatzal provinces are generally consistent with published Nd model ages (Bennett and DePaolo, 1987), however, the Hf crustal model age for Yavapai province is older than equivalent Nd model ages (cf., Fig. 1). Because model ages are calculated based on composition of the material analyzed, there is no conversion required between Nd and Hf model ages. Note that Hf model ages based on zircon (e.g., Lu/Hf = 0.001) rather than crustal compositions are much older.

4.3. Zircon $\delta^{18}O$ results

Results of zircon $\delta^{18}O$ analyses are presented in Table 1, Figs. 4c and 6b, and Supplementary Table 3. Reported weighted mean zircon $\delta^{18}O$ values are calculated from age domains in zircon grains that are interpreted to reflect the crystallization/emplacement age of the sample, based on CL images and prior U-Pb analyses. Most samples have uncertainties of < 1 ‰ for weighted mean values (Table 1). Like the zircon $\varepsilon Hf_{(t)}$ results, there is no clear temporal trend in $\delta^{18}O_{zrc}$ data apart from a subtle increase in the range of $\delta^{18}O$ values and increase in the mean $\delta^{18}O$ value toward the present (Fig. 4c).

Temporal trends are more apparent when the data are plotted against longitude (Fig. 6b). East of ~114 °W longitude, all of the samples analyzed have mantle-like $\delta^{18}O_{zrc}$, although only one sample (Dragoon) older than 40 Ma was analyzed. West of ~114 °W longitude, samples younger than 40 Ma display a shift to higher $\delta^{18}O$ (Fig. 6b) at any specific longitude. This shift is not well-defined (only two samples < 40 Ma are located west of ~ 114 °W longitude), but the shift is consistent with previously published oxygen isotopic data (Fig. 6b; Supplementary Table 4).

Except for samples Dragoon and Cooke, premagmatic zircon age domains were not systematically analyzed for $\delta^{18}O_{zrc}$. Premagmatic age domains in sample Dragoon yielded relatively high $\delta^{18}O_{zrc}$ values (8.8 ± 1.4 ‰; n=4; Supplementary Table 3) relative to zircon rims (6.6 ± 1.6 ‰; Table 1). Premagmatic age domains in sample Cooke yielded relatively low $\delta^{18}O_{zrc}$ values (3.0 ± 0.4 ‰; n=2; Supplementary Table 3) relative to zircon rims (5.1 ± 1.2 ‰; Table 1). Analysis of inherited zircon age domains in samples Dragoon and Cooke yielded U-Pb ages of 1.5-1.6 Ga (Supplementary Table 1), which may be associated with the premagmatic $\delta^{18}O_{zrc}$ values, although the domains analyzed for oxygen isotopes were not directly dated by U-Pb.

5. Discussion

5.1. The origin of spatial trends in radiogenic isotope data

Before attempting to interpret the isotopic results in terms of tectonic events or geodynamic processes, the origin of the spatial trends needs to be evaluated. End-members for factors that could generate the spatial trends in the Hf and Nd isotopic composition of igneous rocks in Fig. 6a are: 1) spatial changes in the degree of crustal (or sediment) assimilation, 2) spatial changes in the isotopic composition of the material assimilated, and 3) spatial changes in the melt source. Except for Laramide-age peraluminous rocks associated with crustal anatexis (Miller and Barton, 1990), the initial melt source for Mesozoic and younger Cordilleran (continental arc) magmatism is interpreted to be the upper mantle (e.g., Farmer and DePaolo, 1984; Hildreth and Moorbath, 1988; Annen et al., 2006). Thus, estimating the isotopic composition of the mantle source can help to distinguish between the end-members listed above.

The radiogenic isotopic composition of the mantle source can be estimated by examining the most primitive or least differentiated (e.g., lowest SiO_2 wt. %) rocks from a particular magmatic suite (Coleman and Glazner, 1997) (Fig. 7b). The most positive $\varepsilon Nd_{(t)}$ values in Fig. 7b can be used as "mantle limit lines" (cf., Miller et al., 2000; Chapman et al., 2017) to help constrain the isotopic composition of the mantle source region. The top of the "> 40 Ma" and "< 40 Ma" bands in Fig. 6a are not strictly mantle limit lines (*sensu* Miller et al., 2000), but their geometry provides a crude approximation to the

mantle isotopic composition. Mantle limit lines that incorporate all data points (*sensu* Miller et al., 2000) could be drawn on Fig. 6a by increasing the top of the "40 Ma" bands by 5-10 epsilon units.

If the longitudinal variation in $\varepsilon Hf_{(t)}$ and $\varepsilon Nd_{(t)}$ in the southwestern U.S. Cordillera was related only to spatial changes in the efficiency of crustal assimilation (end-member 1) or only related to isotopic variations in the crust (i.e., basement terranes) (end-member 2) , then the mantle limit lines in Fig. 7b, or the top of the "40Ma" bands in Fig. 6a, would be expected to be flat (reflecting a single mantle source), rather than sub-parallel to the most negative $\varepsilon Nd_{(t)}$ and $\varepsilon Hf_{(t)}$ values in the isotopic trends in Figs. 6a and 7b. Furthermore, Fig. 7b shows that there is a wide range of rock compositions (SiO_2 wt. %) at all longitudes. If the radiogenic spatial trends were only related to crustal assimilation, then the most mafic samples would be expected to occur in the regions with the highest $\varepsilon Nd_{(t)}$ or $\varepsilon Hf_{(t)}$ values. The isotopic variation at any specific longitude ($\leq$ 10 epsilon units) is primarily related to assimilation of crustal material (Fig. 7b), but the range of the spatial radiogenic isotopic trend across all longitudes (~30 epsilon units) is too large to be explained by changes in the degree of crustal assimilation alone (end-member 1). These observations are consistent with previous studies of the southwestern U.S. Cordillera that suggested spatial trends in isotopic composition principally reflect the composition of the mantle source (Miller et al., 2000; Chapman et al., 2017).

5.2. Mantle Sources

The importance of the mantle source in controlling spatial radiogenic isotopic trends is supported by individual isotopic studies from the southwestern U.S. Cordillera that indicate that, prior to late Miocene lithospheric (Basin and Range) extension, the North American mantle lithosphere remained coupled to the crust and was the primary source of magmatism (Farmer et al., 1995; 2008; DePaolo and Daley, 2000; McMillan et al., 2000). In general, these studies use the evolved radiogenc isotopic compositions of relatively primitive (mafic) igneous rocks infer an evolved mantle source (i.e., the mantle lithosphere).

During Basin and Range extension (~15 Ma to present) there was a widespread shift to more juvenile radiogenic and oxygen isotopic compositions that is attributed to a change in the mantle source region from continental mantle lithosphere to asthenospheric mantle (from isotopically enriched to depleted) as extension progressed (Glazner et al., 1991; Farmer et al., 1995; DePaolo and Daley, 2000; McMillan et al., 2000). These studies provide a base-line for recognizing melts originating in the asthenospheric (depleted) mantle and suggest that prior to Basin and Range extension the mantle lithosphere in many places in the southwestern U.S. Cordillera was largely intact. Dismemberment or removal of mantle lithosphere from the southwestern U.S. Cordillera during the late Miocene to recent was not uniform and in some locations evolved radiogenic isotopes suggest that ancient mantle lithosphere is still preserved in the Basin and Range province (Farmer et al., 1989).

5.2.1. East of ~114 °W longitude

The relationship between the lithosphere and the isotopic composition magmatism is most pronounced on the eastern side (east of ~114 °W longitude) of the U-shaped $\varepsilon Hf_{(t)}$ spatial trend in Fig. 6a. The eastward increase in $\varepsilon Hf_{(t)}$ values mirrors a decrease in basement terrane U-Pb ages and Sm-Nd model ages (Bennett and DePaolo, 1987; Whitmeyer and Karlstrom, 2007) (Fig. 7a). Moreover, $\varepsilon Hf_{(t)}$ values associated with Proterozoic inherited ages (e.g., some zircon cores) and crystallization ages of samples from the Yavapai, Mazatzal, and Grenville crustal provinces (located east of ~ 114 °W longitude) plot along crustal Lu/Hf evolution lines (Fig. 5), which is consistent with melting and assimilation of a lithospheric source of approximately the same age and composition as the lithospheric province exposed at the surface. These observations suggest that the spatial radiogenic isotopic trend east of ~114 °W longitude is primarily related to the age and composition of the lithosphere (including mantle lithosphere).

5.2.2. West of ~114 °W longitude

The nature of mantle sources is also important for interpreting the spatial radiogenic isotopic trend west of ~114 °W longitude (Fig. 6a). The Mojave terrane located west of ~114 °W longitude has

445 the oldest crustal model ages in the southwestern U.S. Cordillera (Wooden et al., 2013; Fig. 1), but $\varepsilon Hf_{(t)}$
446 values of samples from the Mojave terrane are less evolved than expected (< -15 $\varepsilon Hf_{(t)}$) if Mesozoic to
447 Cenozoic igneous rocks were derived from an ancient lithospheric source (the explanation for the spatial
448 isotopic trend east of ~114 °W longitude). In addition, Lu-Hf analyses of Mesozoic to Cenozoic zircon
449 age domains do not plot along crustal evolution lines with Proterozoic zircon age domains from the same
450 grain or sample from the Mojave terrane (Fig. 5). Part of this inconsistency likely reflects complexity in
451 the evolution of the Mojave province (Wooden et al., 2013), but samples > 40 Ma and < 40 Ma both show
452 a westward increase in zircon $\varepsilon Hf_{(t)}$, which is consistent with existing whole rock Nd and Sr isotopic data
453 from the Mojave region (Glazner and O'Neil, 1989; Miller et al., 2000) (Fig. 6a).
454 Previous studies have suggested that this westward transition to more juvenile isotopic values
455 reflects a transition from continental mantle lithosphere to juvenile depleted asthenosphere or oceanic
456 mantle lithosphere as the mantle source (Glazner and O'Neil, 1989; Miller et al., 2000; Chapman et al.,
457 2017). Chapman et al. (2017) suggested that this transition in the southwest U.S. Cordillera is an intrinsic
458 feature of continental arcs and Cordilleran orogens globally and reflects systematic removal of mantle
459 lithosphere and possibly lower crust close to the subduction interface.
460

461 ## 5.3. Temporal trends in radiogenic isotopic data

462 Following the above interpretations, the change in slope (from negative to positive) of the $\varepsilon Hf_{(t)}$
463 and $\varepsilon Nd_{(t)}$ trends in in Fig. 6a can be used to roughly estimate the position of the edge of intact North
464 America mantle lithosphere and how that feature may have changed through time. For samples older than
465 40 Ma, the lowest $\varepsilon Hf_{(t)}$ values, and interpreted western edge of intact continental mantle lithosphere,
466 occur at 117 °W to 116 °W longitude (Fig. 6a). West of this longitude, the mantle lithosphere is
467 interpreted to have gradually thinned toward the trench, consistent with previous isotopic studies that
468 suggested the mantle lithosphere was thin to absent in the westermost Mojave region during the Jurassic
469 (Miller et al., 1995; Miller and Glazner, 1995) (Fig. 2a-b). South of the study area, evolved isotope ratios
470 suggest that continental mantle lithosphere extended to at least the present-day location of the San

Andreas Fault during the Late Cretaceous (Barth et al., 2016). Dense sampling of the Peninsular Ranges batholith (on the west side of the San Andreas Fault, Fig. 1) indicates that during the Cretaceous, the transition to more juvenile isotopic compositions occurred across a horizontal distance of as little as ~50 km at this location (Kistler et al., 2003).

Continental mantle lithosphere was the likely source for Jurassic igneous rocks east of ~116 °W longitude (e.g., Rämö et al., 2002) (Fig. 2a). The approximate western edge of intact mantle lithosphere after 40 Ma is interpreted to be located between 114 °W and 113 °W longitude (Figs. 2c and 7). Previous isotopic studies of volcanic rocks in the Mojave region suggested that the western edge of intact mantle lithosphere extended to ~116 °W longitude during the early to middle Miocene (Glazner and O'Neil, 1989; Miller et al., 2000). The shift in the position of the western edge of intact North American mantle lithosphere suggests that a large segment (200-400 km in width, not restored for contraction or extension) of the mantle lithosphere was thinned and/or removed by 40 Ma. The thin dashed line labeled, "future LAB" in cross-section X (Fig. 2b) marks the region of the mantle lithosphere and possibly lower crust that is hypothesized to have been removed during the Laramide orogeny. Cross-section Y (Fig. 2c) shows the position of the edge of intact mantle lithosphere (heavy vertical dashed line) has shifted eastward in comparison to cross-section X. The loss or partial removal of mantle lithosphere has been previously associated with low-angle to flat-slab subduction during the Laramide orogeny (Miller et al., 2000; Saleeby, 2003). Surface exposures of the Pelona-Orocopia-Rand schist (associated with Laramide shallow subduction) occur as far east as ~113.5 °W (Fig. 6b; Chapman, 2017), comparable to the estimated western edge of post-40 Ma intact mantle lithosphere (Fig. 2c-d).

5.4. Zircon oxygen isotopes

Similar to the radiogenic isotopic data, there are differences in zircon oxygen isotopes east and west of ~114 °W longitude and before and after ~40 Ma. East of ~114 °W longitude, all of the samples analyzed have mantle-like $\delta^{18}O_{zrc}$ (Fig. 6b), consistent with a mantle source (Eiler, 2001) that is interpreted to be the continental mantle lithosphere and suggests limited assimilation of crustal material.

There paucity of samples > 40 Ma located east of ~114 °W longitude make it difficult to assess temporal changes, but it appears as if there is little difference in $\delta^{18}O_{zrc}$.

West of ~114 °W longitude, $\delta^{18}O_{zrc}$ generally decreases from west to east (Fig. 6b). This contrasts with the central U.S. Cordillera where $\delta^{18}O_{zrc}$ generally increases from west to east (King et al., 2004). In the central U.S. Cordillera, oxygen isotope ratios increase east of the $^{87}Sr/^{86}Sr = 0.706$ line and high $\delta^{18}O_{zrc}$ is believed to be related to assimilation of crustal material (King et al., 2004). The highest $\delta^{18}O_{zrc}$ values in the central U.S. Cordillera correspond to the regions with the thickest Paleozoic passive margin sequence (Cordilleran miogeocline; Stewart, 2005) and $\delta^{18}O_{zrc}$ was slightly higher during the Cretaceous, when the crust is believed to have been the thickest, which may favor crustal assimilation (King et al., 2004). The Cordilleran miogeocline is present in the westernmost Mojave region (Stewart, 2005) and correlates with the position of the highest $\delta^{18}O$ in the southwestern U.S. Cordillera prior to 40 Ma (Figs. 2b and 6b). Values of $\delta^{18}O$ for igneous rocks older than 40 Ma in the Mojave region are only slightly higher than mantle values (Fig. 6b). The spatial pattern of $\delta^{18}O$ in the Sierra Nevada is more complex (Lackey et al., 2008) and particularly high $\delta^{18}O_{zrc}$ (> 8 ‰) in the southern Sierra Nevada (Fig. 6b) has been attributed to underthrust altered oceanic and volcanic crust during exotic terrane accretion (Lackey et al., 2005).

There is a pronounced temporal shift to higher $\delta^{18}O$ after ~40 Ma in samples located west of ~114 °W longitude (Fig. 6b). Glazner and O'Neil (1989) suggested that high whole rock $\delta^{18}O$ (equivalent to > 8 ‰ $\delta^{18}O_{zrc}$, calibrated for the SiO_2 wt. % of the whole rock; Lackey et al., 2008) for Miocene volcanic rocks west of ~116 °W longitude was caused by melting and assimilation of underplated Pelona-Orocopia-Rand schist. The Pelona-Orocopia-Rand schist has relatively juvenile $\varepsilon Nd_{(t)}$ compositions and relatively heavy $\delta^{18}O$ compositions (Glazner and O'Neil, 1989). The results of this study are consistent with that interpretation and indicate that Mesozoic to early Cenozoic igneous rocks in the Mojave region are characterized by relatively lower $\delta^{18}O_{zrc}$ ($\leq$ 7 ‰) (Figs. 6b). Because the Pelona-Orocopia-Rand sediments were emplaced before ~40 Ma (Grove et al., 2003), the relatively heavy $\delta^{18}O$ of Miocene rocks is likely related to partial melting and assimilation of Pelona-Orocopia-Rand schist in the lower crust, rather than introduction of high $\delta^{18}O$ material into the mantle source region during subduction. Also,

because Miocene igneous rock suites in the Mojave are metaluminous and extend to mafic compositions (Miller et al., 2000), single-stage melting of the Pelona-Orocopia-Rand schist (crustal anatexis), without precursory partial melting of the mantle is unlikely.

5.5. Interpreting isotopic trends from Cordilleran orogenic systems

One of the central implications of this study is that the isotopic composition of igneous rocks in Cordilleran orogens may not always record changes in tectonic processes or geodynamics and that the age and composition of the lithosphere hosting the magmatic products should be considered. The absence of a temporal shift in isotopic compositions east of ~114 °W longitude (Fig. 6) suggests that continental mantle lithosphere was the predominant mantle source for Mesozoic to early Miocene magmas. As magmatism migrated back and forth across the Cordillera east of ~114 °W longitude (e.g., Fig. 3), the isotopic composition of magmatism at a specific geographic location remained relatively constant through time (Fig. 6a). Events that generated nearly contemporaneous magmatism at different longitudes, such as the ignimbrite flare-up, had isotopic values that reflect the age and composition of the local lithosphere. Variation in radiogenic isotopic composition at a specific geographic location is generally ≤ 10 $\varepsilon Hf_{(t)}$ and most of that variation appears related to differentiation and assimilation within the crust (Fig. 7b), which may be independent of the tectonic or geodynamic conditions at the time. Despite changes in subduction zone dynamics (low-angle subduction, slab-rollback, slab foundering) and a transition from a contractional to extensional tectonic regime, there are not large (>10 $\varepsilon Hf_{(t)}$) changes in the isotopic composition of magmatism east of ~114 °W longitude.

Tectonic processes do appear to have influenced radiogenic and stable (oxygen) isotopic compositions west of ~114 °W longitude (Fig. 6), but not in the ways envisioned by Kemp et al. (2009) for accretionary orogens, which have been applied to Cordilleran orogens such as the Andes (e.g., Boekhout et al., 2015). A shift to more juvenile radiogenic isotopes west of ~114 °W longitude for samples < 40 Ma suggests that the mantle lithosphere was thinned or partially removed and replaced by depleted mantle (presumably either asthenosphere or young oceanic mantle lithosphere). This shift is not

550 directly related to periods of extension or crustal thinning. These results suggest that crustal processes
551 that do not involve removal or modification of the mantle lithosphere (e.g., crustal shortening and
552 thickening) may not be easily resolvable in the radiogenic isotopic record.

553 Zircon $\delta^{18}O$ data from west of ~114 °W longitude may also not be directly related to tectonic
554 processes. The relatively large (2-4 ‰) post 40 Ma shift to heavier $\delta^{18}O$ (Fig. 6b) is interpreted to reflect
555 extensive underplating of sediment during shallow subduction (Fig. 2). Crustal thickening accompanied
556 shallow subduction during the Laramide orogeny and may have enhanced crustal assimilation, leading to
557 larger $\delta^{18}O_{zrc}$ values, but periods of contraction in Cordilleran orogens are not always associated with low-
558 angle subduction or sediment underplating. Smaller variations in $\delta^{18}O_{zrc}$ ($\leq$ 2 ‰) may be related to the
559 degree of crustal assimilation, however, spatial variations in $\delta^{18}O$ (e.g., increasing toward the trench; Fig.
560 6b) appear to be pronounced for samples > 40 Ma as well.

561 The results of this study suggest that the geographic distribution of magmatism should be
562 considered when interpreting tectonic events or geodynamic processes from igneous isotopic data.
563 Detrital isotopic data (e.g., zircon Lu-Hf) may be particularly susceptible to misinterpretation. For
564 example, during the Laramide orogeny in the southwestern U.S. Cordillera the locus of magmatism
565 migrated eastward into increasingly isotopically juvenile crustal provinces. This was a period of
566 contraction and crustal thickening, however, zircon $\varepsilon Hf_{(t)}$ data from this event would record a temporal
567 trend to more juvenile compositions.

568 The best way to interpret specific tectonic events from isotopic data may be to focus on a limited
569 geographic area that is less likely to be affected by regional isotopic trends. We present such an analysis
570 for the Mojave Desert region in Fig. 8. During the Jurassic to Late Cretaceous, the radiogenic isotopic
571 composition of magmatism was relatively evolved, reflecting an enriched continental mantle lithosphere
572 source, consistent with mantle-like zircon oxygen isotope ratios (<7 ‰ $\delta^{18}O_{zrc}$). The slightly more
573 negative $\varepsilon Hf_{(t)}$ in the Late Cretaceous, compared to the Jurassic and Early Cretaceous (Fig. 8), may reflect
574 more efficient crustal assimilation in thicker crust associated with retroarc shortening (Spencer and
575 Reynolds, 1990). Alternatively, these shifts may reflect changes in the lithospheric mantle source,
576 changes within the Mojave province lower crust, or changes at the crust-mantle boundary, as the arc

577 evolved (Barth and Wooden, 2010; Barth et al., 2016). Slightly higher $\delta^{18}O_{zrc}$ in the Late Cretaceous is
578 also consistent with more efficient crustal assimilation. During the Laramide orogeny, the North
579 American mantle lithosphere (radiogenically enriched peridotite) in the Mojave Desert region is
580 interpreted to have been at least partially replaced by young oceanic lithosphere (isotopically depleted
581 mafic crust and peridotite) or asthenospheric mantle (isotopically depleted peridotite) (Miller et al., 2000)
582 (Fig. 2c-d), causing $\varepsilon Hf_{(t)}$ to increase in early Miocene igneous rocks (Fig. 8). A concurrent increase in
583 $\delta^{18}O$ in the Mojave Desert region is interpreted to reflect partial melting and assimilation of Pelona-
584 Orocopia-Rand schist within the lower crust (Glazner and O'Neil, 1989) (Fig. 2d; 8). During the early
585 Miocene to the Quaternary, $\delta^{18}O$ returns to mantle-like compositions (~ 6 ‰) and radiogenic isotope
586 ratios shift to more isotopically juvenile compositions (~ +10 $\varepsilon Hf_{(t)}$), both of which are consistent with
587 partial melting of the asthenospheric mantle with minimal crustal assimilation during Basin and Range
588 lithospheric extension (Glazner et al., 1991) (Fig. 8). Detrital zircon from a hypothetical sandstone,
589 whose sediment source region was located entirely in the area examined in Fig. 8, could accurately record
590 temporal changes in isotopic composition and could be used to more confidently identify and interpret
591 tectonic processes.
592

593 # 6. Conclusions

594 This study is the first regional zircon $\varepsilon Hf_{(t)}$ and $\delta^{18}O_{zrc}$ dataset for Mesozoic to early Miocene
595 igneous rocks in the southwestern U.S. Cordillera. We recognize orogen-scale spatial and temporal
596 isotopic trends, interpret the origin of those trends, and integrate the isotopic data into the geologic history
597 of the region. The results are used to evaluate and improve the use of zircon isotopic data to interpret
598 tectonic events and geodynamics processes in Cordilleran orogens

599 When plotted against longitude (sub-parallel to the orogenic structural grain) zircon $\varepsilon Hf_{(t)}$ data
600 form a U-shaped isotopic trend with a minimum at ~114 °W longitude and increases toward the east and
601 west (Fig. 6a). The eastern limb of the U-shaped zircon $\varepsilon Hf_{(t)}$ trend is interpreted to reflect an eastward
602 decrease in the age of lithospheric provinces (Figs. 1 and 7a). Zircon $\varepsilon Hf_{(t)}$ from inherited cores plot

along mean crustal Lu/Hf evolution lines (Fig. 5), consistent with partial melting of the same lithospheric source through time. Zircon $\delta^{18}O$ east of ~114 °W longitude is similar in composition to mantle-derived zircon and indicates limited crustal assimilation in Mesozoic to recent igneous rocks (Fig. 6b). Correlation of whole rock SiO_2 (wt. %) with radiogenic isotope ratios (Fig. 7b) suggests that the continental mantle lithosphere was the mantle source for the majority of Mesozoic to early Miocene igneous rocks in the eastern limb of the U-shaped trend (Fig. 2). East of ~114 °W longitude, there is no significant isotopic difference between magmatism associated with shallow to flat-slab subduction and crustal thickening during the Laramide orogeny and magmatism associated with subduction roll-back or foundering of the Farallon slab and crustal extension following the Laramide orogeny (Fig. 2). These results indicate that subduction dynamics and orogenic processes may not always be resolvable in the zircon $\varepsilon Hf_{(t)}$ record. The largest temporal changes in zircon $\varepsilon Hf_{(t)}$ are related to the migration of magmatism into different lithospheric provinces (basement terranes) rather than periods of contraction or extension.

The western limb of the U-shaped zircon $\varepsilon Hf_{(t)}$ trend (Fig. 6a) is interpreted to reflect a transition from intact North American continental mantle lithosphere in the east to a depleted asthenospheric or oceanic lithospheric mantle source region in the west (Figs. 2 and 7a). The minimum, or change in slope, of the U-shaped trend (Fig. 6a) is used to estimate the position of the western edge of intact continental mantle lithosphere through time (Fig. 2). Prior to the Laramide orogeny (>40 Ma), the edge of intact mantle lithosphere was located at 116-117 °W longitude (present-day coordinates) (Figs. 2a-b and 6a). There is a shift to more juvenile zircon $\varepsilon Hf_{(t)}$ for samples <40 Ma and the minimum of the U-shaped isotopic trend moves eastward. The < 40 Ma isotopic shift is attributed to partial removal or replacement of a portion of the continental mantle lithosphere in the Mojave region during the Laramide orogeny and the edge of intact continental mantle is interpreted to have moved to ~114 °W longitude (present-day coordinates) (Figs. 2c-d, 6a). There is also a shift to significantly higher $\delta^{18}O$ in samples younger than 40 Ma, which is attributed to lower crustal assimilation of Pelona-Orocopia-Rand schist that was underplated during the Laramide orogeny (Figs. 2c-d, 6b). These results suggest that changes in the composition of the upper mantle (e.g., from evolved continental mantle lithosphere to depleted asthenospheric mantle)

630 have the greatest influence on the radiogenic isotopic composition of Cordilleran magmatism. The
631 influence of crustal processes, like thickening or thinning, are less pronounced and may be obscured by
632 spatial trends or differences in the efficiency or amount of crustal assimilation, which may be responsible
633 for ≤ 10 zircon $\varepsilon Hf_{(t)}$ shifts at any specific location in the orogen.

634 The isotopic data from the southwestern U.S. Cordillera show that spatial and temporal zircon
635 isotopic trends can be an effective tool to monitor changes in the composition or architecture of the
636 mantle source region and have applications for interpreting past geodynamic processes such as subduction
637 erosion, delamination of the mantle lithosphere, and sediment underplating. However, regional (spatial)
638 trends in isotopic composition related to lithospheric composition are significantly larger than temporal
639 trends associated with tectonic processes in both the mantle and crust. Distinguishing tectonic events
640 from arc migration in Cordilleran orogens using detrital zircon datasets is particularly difficult without
641 information on the sediment source area. Limiting the geographic scope of zircon isotopic investigations
642 (Fig. 8) is one way to help avoid conflating spatial and temporal isotopic trends.

643

644 ## Acknowledgements

645 Funding was provided by an EarthScope award for Geochronology Student Research (AGeS) (J.C.), a
646 University of Arizona Graduate and Professional Student Council (GPSC) grant (J.C.), and the Romanian
647 Executive Agency for Higher Education, Research, Development and Innovation Funding project PN-III-
648 P4-ID-PCE-2016-0127 (M.N.D.). Support for the University of Arizona Laserchron center comes from
649 NSF EAR 1338583 and NSF EAR 1649254 (G.G.). WiscSIMS is supported by NSF EAR 1355590 and
650 UW Madison (J.V.). J.D. Mizer provided zircon mounts for previously dated samples. Constructive
651 reviews and comments from editor Aaron Cavosie, associate editor Chris Kirkland, Jon Spencer, Andy
652 Barth, and Paul Wetmore helped to improve the manuscript.

653

654 ## References:

655 Annen, C., Blundy, J. D., & Sparks, R. S. J. (2006). The genesis of intermediate and silicic magmas in
656 deep crustal hot zones. Journal of Petrology, 47(3), 505-539.
657 Armstrong, R.L. and Ward, P., 1991, Evolving geographic patterns of Cenozoic magmatism in the North
658 American Cordillera: The temporal and spatial association of magmatism and metamorphic core
659 complexes: Journal of Geophysical Research: Solid Earth, v. 96, p. 13201-13224.
660 Atwater, T., and Stock, J., 1998, Pacific-North America plate tectonics of the Neogene southwestern
661 United States: an update. International Geology Review, v. 40, p. 375-402.
662 Balgord, E.A., 2017, Triassic to Neogene evolution of the south-central Andean arc determined by detrital
663 zircon U-Pb and Hf analysis of Neuquén Basin strata, central Argentina (34° S–40° S):
664 Lithosphere, v. 9, p.453-462.
665 Barth, A.P. and Wooden, J.L., 2006. Timing of magmatism following initial convergence at a passive
666 margin, southwestern US Cordillera, and ages of lower crustal magma sources. The Journal of
667 Geology, 114(2), pp.231-245.
668 Barth, A.P., Wooden, J.L., Jacobson, C.E. and Probst, K., 2004. U-Pb geochronology and geochemistry
669 of the McCoy Mountains Formation, southeastern California: A Cretaceous retroarc foreland
670 basin. Geological Society of America Bulletin, 116(1-2), pp.142-153.
671 Barth, A.P., Wooden, J.L., Miller, D.M., Howard, K.A., Fox, L.K., Schermer, E.R. and Jacobson, C.E.,
672 2017, Regional and temporal variability of melts during a Cordilleran magma pulse: Age and
673 chemical evolution of the Jurassic arc, eastern Mojave Desert, California: Geological Society of
674 America Bulletin, v. 129, p. 429-448.
675 Bennett, V.C. and DePaolo, D.J., 1987, Proterozoic crustal history of the western United States as
676 determined by neodymium isotopic mapping: Geological Society of America Bulletin, v. 99, p.
677 674-685.
678 Bindeman, I.N. and Valley, J.W., 2001, Low-$\delta^{18}O$ rhyolites from Yellowstone: Magmatic evolution based
679 on analyses of zircons and individual phenocrysts: Journal of Petrology, v. 42, p. 1491-1517.
680 Boekhout, F., Roberts, N.M., Gerdes, A., and Schaltegger, U., 2015, A Hf-isotope perspective on
681 continent formation in the south Peruvian Andes, in Roberts, N., Van Kranendonk, M., Parman,

682 S., Shirey, S., and Clift, P.D., eds., Continent Formation Through Time: Geological Society,
683 London, Special Publication 389, p. 305-321.
684 Bouvier, A., Vervoort, J.D. and Patchett, P.J., 2008, The Lu–Hf and Sm–Nd isotopic composition of
685 CHUR: constraints from unequilibrated chondrites and implications for the bulk composition of
686 terrestrial planets: Earth and Planetary Science Letters, v. 273, p. 48-57.
687 Busby, C.J., 2012, Extensional and transtensional continental arc basins: Case studies from the
688 southwestern United States, in Tectonics of Sedimentary Basins: Recent Advances (eds. Busby,
689 C., and Azor, A.) John Wiley & Sons, Ltd., Chichester, UK, p. 382-404.
690 Cecil, M.R., Gehrels, G., Ducea, M.N. and Patchett, P.J., 2011, U-Pb-Hf characterization of the central
691 Coast Mountains batholith: Implications for petrogenesis and crustal architecture: Lithosphere, v.
692 3, p.247-260.
693 Cecil, M.R., Rotberg, G.L., Ducea, M.N., Saleeby, J.B., and Gehrels, G.E., 2012, Magmatic growth and
694 batholithic root development in the northern Sierra Nevada, California: Geosphere, v. 8, p. 592-
695 606.
696 Chapman, A.D., 2017, The Pelona–Orocopia–Rand and related schists of southern California: a review of
697 the best-known archive of shallow subduction on the planet: International Geology Review, v. 59,
698 p. 664-701.
699 Chapman, J.B., Ducea, M.N., Kapp, P., Gehrels, G.E. and DeCelles, P.G., 2017, Spatial and temporal
700 radiogenic isotopic trends of magmatism in Cordilleran orogens: Gondwana Research, v. 48, p.
701 189-204.
702 Clinkscales, C.A., and Lawton, T.F., 2015, Timing of Late Cretaceous shortening and basin development,
703 Little Hatchet Mountains, southwestern New Mexico, USA–implications for regional Laramide
704 tectonics: Basin Research, v. 27, p. 453-472.
705 Coleman, D.S. and Glazner, A.F., 1997, The Sierra Crest magmatic event: Rapid formation of juvenile
706 crust during the Late Cretaceous in California: International Geology Review, v. 39, p.768-787.
707 Coney, P.J. and Reynolds, S.J., 1977, Cordilleran benioff zones: Nature, v. 270, p. 403-406.

708 Constenius, K.N., Esser, R.P. and Layer, P.W., 2003, Extensional collapse of the Charleston-Nebo salient
709 and its relationship to space-time variations in Cordilleran orogenic belt tectonism and continental
710 stratigraphy, in Cenozoic systems of the Rocky Mountain Region (eds. Raynolds, R.G. and
711 Flores, R.M.), Denver, CO: Rocky Mountain Section SEPM, p. 303-353.
712 Davis, G.H., 1979, Laramide folding and faulting in southeastern Arizona: American Journal of Science,
713 v. 279, p. 543-569.
714 DeCelles, P.G., 2004, Late Jurassic to Eocene evolution of the Cordilleran thrust belt and foreland basin
715 system, western USA: American Journal of Science, v. 304, p. 105-168.
716 DeCelles, P.G., and Graham, S.A., 2015, Cyclical processes in the North American Cordilleran orogenic
717 system: Geology, v. 43, p. 499-502.
718 DeCelles, P.G., Ducea, M.N., Kapp, P. and Zandt, G., 2009, Cyclicity in Cordilleran orogenic systems:
719 Nature Geoscience, v. 2, p.251.
720 DePaolo, D.J. and Daley, E.E., 2000, Neodymium isotopes in basalts of the southwest basin and range
721 and lithospheric thinning during continental extension: Chemical Geology, v. 169, p.157-185.
722 Dickinson, W.R., 1991, Tectonic setting of faulted Tertiary strata associated with the Catalina core
723 complex in southern Arizona: Geological Society of America Special Paper 264, 106p.
724 Dickinson, W.R., 2004, Evolution of the North American Cordillera. Annual Review of Earth and
725 Planetary Sciences, v. 32, p. 13-45.
726 Dickinson, W.R., and Lawton, T.F., 2001a, Tectonic setting and sandstone petrofacies of the Bisbee basin
727 (USA–Mexico): Journal of South American Earth Sciences, v. 14, p. 475-504.
728 Dickinson, W.R., and Lawton, T.F., 2001b, Carboniferous to Cretaceous assembly and fragmentation of
729 Mexico: Geological Society of America Bulletin, v. 113, p. 1142-1160.
730 Dickinson, W.R., Klute, M.A., Hayes, M.J., Janecke, S.U., Lundin, E.R., McKittrick, M.A., and Olivares,
731 M.D., 1988, Paleogeographic and paleotectonic setting of Laramide sedimentary basins in the
732 central Rocky Mountain region: Geological Society of America Bulletin, v. 100, p. 1023-1039.
733 Ducea, M., 2001, The California arc: Thick granitic batholiths, eclogitic residues, lithospheric-scale
734 thrusting, and magmatic flare-ups: GSA Today, v. 11, p. 4-10.

735 Ducea, M., and Saleeby, J., 1998, A case for delamination of the deep batholithic crust beneath the Sierra
736 Nevada, California: International Geology Review, v. 40, p. 78-93.
737 Ducea, M.N. and Barton, M.D., 2007, Igniting flare-up events in Cordilleran arcs: Geology, v. 35, p.
738 1047-1050.
739 Ducea, M.N., Kidder, S., Chesley, J.T., and Saleeby, J.B., 2009, Tectonic underplating of trench
740 sediments beneath magmatic arcs: The central California example: International Geology
741 Review, v. 51, p.1-26.
742 Ducea, M.N., Saleeby, J.B., and Bergantz, G., 2015, The architecture, chemistry, and evolution of
743 continental magmatic arcs: Annual Review of Earth and Planetary Sciences, v. 43, p. 299-331.
744 Dunne, G.C. and Walker, J.D., 2004. Structure and evolution of the East Sierran thrust system, east
745 central California. Tectonics, 23(4).
746 Eiler, J. M., 2001, Oxygen isotope variations of basaltic lavas and upper mantle rocks: Reviews in
747 Mineralogy and Geochemistry, v. 43, v. 319-364.
748 Farmer, G.L., and DePaolo, D.J., 1984, Origin of Mesozoic and Tertiary granite in the western United
749 States and implications for Pre-Mesozoic crustal structure: 2. Nd and Sr isotopic studies of
750 unmineralized and Cu-and Mo-mineralized granite in the Precambrian Craton: Journal of
751 Geophysical Research: Solid Earth, v. 89, p. 10141-10160.
752 Farmer, G.L., Bailley, T., and Elkins-Tanton, L.T., 2008, Mantle source volumes and the origin of the
753 mid-Tertiary ignimbrite flare-up in the southern Rocky Mountains, western U.S.: Lithos, v. 102,
754 p. 279-294.
755 Farmer, G.L., Glazner, A.F., Wilshire, H.G., Wooden, J.L., Pickthorn, W.J., and Katz, M., 1995, Origin
756 of late Cenozoic basalts at the Cima volcanic field, Mojave Desert, California: Journal of
757 Geophysical Research: Solid Earth, v. 100, p. 8399-8415.
758 Farmer, G.L., Perry, F.V., Semken, S., Crowe, B., Curtis, D., and DePaolo, D.J., 1989, Isotopic evidence
759 on the structure and origin of subcontinental lithospheric mantle in southern Nevada: Journal of
760 Geophysical Research: Solid Earth, v. 94, p. 7885-7898.

761 Fitz-Díaz, E., Lawton, T. F., Juárez-Arriaga, E., and Chávez-Cabello, G., 2017, The Cretaceous-
762 Paleogene Mexican orogen: Structure, basin development, magmatism and tectonics: Earth-
763 Science Reviews, doi.org/10.1016/j.earscirev.2017.03.002.
764 Gehrels, G. and Pecha, M., 2014, Detrital zircon U-Pb geochronology and Hf isotope geochemistry of
765 Paleozoic and Triassic passive margin strata of western North America: Geosphere, v. 10, p. 49-
766 65.
767 Gehrels, G.E., Valencia, V.A. and Ruiz, J., 2008, Enhanced precision, accuracy, efficiency, and spatial
768 resolution of U-Pb ages by laser ablation–multicollector–inductively coupled plasma–mass
769 spectrometry: Geochemistry, Geophysics, Geosystems, v. 9, doi:10.1029/2007GC001805.
770 Glazner, A.F., and O'Neil, J.R., 1989, Crustal structure of the Mojave Desert, California: Inferences from
771 Sr and O Isotope studies of Miocene volcanic rocks: Journal of Geophysical Research, v. 94, p.
772 7861-7870.
773 Glazner, A.F., Farmer, G.L., Hughes, W.T., Wooden, J., and Pickthorn, W., 1991, Contamination of
774 basaltic magma by mafic crust at Amboy and Pisgah Craters, Mojave Desert, California: Journal
775 of Geophysical Research: Solid Earth, v. 96, p. 13673-13691.
776 Grove, M., Jacobson, C.E., Barth, A.P., and Vucic, A., 2003, Temporal and spatial trends of Late
777 Cretaceous-early Tertiary underplating of Pelona and related schist beneath southern California
778 and southwestern Arizona, in Johnson, S.E., ed., Tectonic evolution of northwestern Mexico and
779 southwestern USA: Geological Society of America Special Paper 374, p. 381-406.
780 Haschke, M., Siebel, W., Günther, A., and Scheuber, E., 2002, Repeated crustal thickening and recycling
781 during the Andean orogeny in north Chile (21–26 S): Journal of Geophysical Research: Solid
782 Earth, v. 107. doi: 10.1029/2001JB000328.
783 Hildreth, W. and Moorbath, S., 1988. Crustal contributions to arc magmatism in the Andes of central
784 Chile. Contributions to mineralogy and petrology, 98(4), pp.455-489.
785 Humphreys, E.D., 1995, Post-Laramide removal of the Farallon slab, western United States: Geology, v.
786 23, p. 987-990.

787 Kemp, A.I.S., Hawkesworth, C.J., Collins, W.J., Gray, C.M., and Blevin, P.L., 2009, Isotopic evidence
788 for rapid continental growth in an extensional accretionary orogen: The Tasmanides, eastern
789 Australia: Earth and Planetary Science Letters, v. 284, p. 455-466.
790 King, E.M., Valley, J.W., Stockli, D.F., and Wright, J.E., 2004, Oxygen isotope trends of granitic
791 magmatism in the Great Basin: Location of the Precambrian craton boundary as reflected in
792 zircons: Geological Society of America Bulletin, v. 116, p.451-462.
793 Kinny, P.D., and Maas, R., 2003, Lu–Hf and Sm–Nd isotope systems in zircon, in Hanchar, J.M., and
794 Hoskin, P.W.O., eds., Zircon: Reviews in Mineralogy and Geochemistry, v. 53, p. 327-341.
795 Kistler, R.W., 1990, Two different lithosphere types in the Sierra Nevada, California, in Anderson J.L.,
796 ed., The nature and origin of Cordilleran magmatism: Boulder, Colorado, Geological Society of
797 America Memoir 174, p. 271-282.
798 Kistler, R.W., and Peterman, Z.E., 1973, Variations in Sr, Rb, K, Na, and initial Sr^{87}/Sr^{86} in Mesozoic
799 granitic rocks and intruded wall rocks in central California: Geological Society of America
800 Bulletin, v. 84, p. 3489-3512.
801 Kistler, R.W., Wooden, J.L. and Morton, D.M., 2003, Isotopes and ages in the northern Peninsular
802 Ranges batholith, southern California: U.S. Geological Survey Open File Report 2003-489, 45p.
803 Kita, N.T., Ushikubo, T., Fu, B., and Valley, J.W., 2009, High precision SIMS oxygen isotope analysis
804 and the effect of sample topography: Chemical Geology, v. 264, p. 43-57.
805 Lackey, J.S., Valley, J.W., and Saleeby, J.B., 2005, Supracrustal input to magmas in the deep crust of
806 Sierra Nevada batholith: evidence from high-$\delta^{18}O$ zircon: Earth and Planetary Science Letters, v.
807 235, p. 315-330.
808 Lackey, J.S., Valley, J.W., Chen, J.H., and Stockli, D.F., 2008, Dynamic magma systems, crustal
809 recycling, and alteration in the central Sierra Nevada batholith: the oxygen isotope record: Journal
810 of Petrology, v. 49, p. 1397-1426.
811 Lang, J.R., and Titley, S.R., 1998, Isotopic and geochemical characteristics of Laramide magmatic
812 systems in Arizona and implications for the genesis of porphyry copper deposits: Economic
813 Geology, v. 93, p. 138-170.

814 Lawton, T.F., and McMillan, N.J., 1999, Arc abandonment as a cause for passive continental rifting:
815 Comparison of the Jurassic Mexican Borderland rift and the Cenozoic Rio Grande rift: Geology,
816 v. 27, p. 779-782.
817 Leveille, R.A., and Stegen, R.J., 2012, The southwestern North America porphyry copper province, in
818 Hedenquist J.W., Harris, M., and Camus, F., eds., Geology and genesis of major copper deposits
819 and districts of the world: a tribute to Richard H. Sillitoe: Society of Economic Geologists,
820 Littleton, Colorado, Special Publication 16, p. 361-401.
821 Lipman, P.W., 1992, Magmatism in the Cordilleran United States; progress and problems, in Burchfiel,
822 B.C., Lipman, P.W., and Zoback, M.L. eds., The Cordilleran Orogen: Conterminous U.S. The
823 Geology of North America: Geological Society of America, Boulder, Colorado, p. 481–514.
824 Liu, L., Gurnis, M., Seton, M., Saleeby, J., Müller, R.D., and Jackson, J.M., 2010, The role of oceanic
825 plateau subduction in the Laramide orogeny: Nature Geoscience, v. 3, p. 353.
826 Martin, M.W., and Walker, J.D., 1992, Extending the western North American Proterozoic and Paleozoic
827 continental crust through the Mojave Desert: Geology, v. 20, p. 753-756.
828 Martini, M., Solari, L., and López-Martínez, M., 2014, Correlating the Arperos Basin from Guanajuato,
829 central Mexico, to Santo Tomás, southern Mexico: Implications for the paleogeography and
830 origin of the Guerrero terrane: Geosphere, v. 10, p. 1385-1401, doi:10.1130/GES01055.1.
831 McMillan, N.J., 2004, Magmatic record of Laramide subduction and the transition to Tertiary extension:
832 Upper Cretaceous through Eocene igneous rocks of New Mexico, in The Geology of New
833 Mexico: a Geologic History (eds., Mack G.H., and Giles, K.A.): New Mexico Geological Society
834 Special Publication 11, p. 249-267.
835 McMillan, N.J., Dickin, A.P., and Haag, D., 2000, Evolution of magma source regions in the Rio Grande
836 rift, southern New Mexico: Geological Society of America Bulletin, v. 112, p. 1582-1593.
837 McQuarrie, N., and Wernicke, B.P., 2005, An animated tectonic reconstruction of southwestern North
838 America since 36 Ma: Geosphere, v. 1, p. 147-172.

839 Miller, C.F., and Barton, M.D., 1990, Phanerozoic plutonism in the Cordilleran interior, USA, in Kay
840 S.M., Rapela, C.W., eds., Plutonism from Antarctica to Alaska: Boulder, Colorado, Geological
841 Society of America Special Paper 241, p. 213-231.
842 Miller, J.S. and Glazner, A.F., 1995, Jurassic plutonism and crustal evolution in the central Mojave
843 Desert, California: Contributions to Mineralogy and Petrology, v. 118, p. 379-395.
844 Miller, J.S., Glazner, A.F., Farmer, G.L., Suayah, I.B., and Keith, L.A., 2000, A Sr, Nd, and Pb isotopic
845 study of mantle domains and crustal structure from Miocene volcanic rocks in the Mojave Desert,
846 California: Geological Society of America Bulletin, v. 112, p. 1264-1279.
847 Miller, J.S., Glazner, A.F., Walker, J.D., and Martin, M.W., 1995, Geochronologic and isotopic evidence
848 for Triassic-Jurassic emplacement of the eugeoclinal allochthon in the Mojave Desert region,
849 California: Geological Society of America Bulletin, v. 107, p. 1441-1457.
850 Rämö, T.O., Calzia, J.P., and Kosunen, P.J., 2002, Geochemistry of Mesozoic plutons, southern Death
851 Valley region, California: Insights into the origin of Cordilleran interior magmatism:
852 Contributions to Mineralogy and Petrology, v. 143, p. 416-437.
853 Ramos, V.A., 2009, Anatomy and global context of the Andes: Main geologic features and the Andean
854 orogenic cycle, in Kay, S.M., Ramos, V.A., and Dickinson, W.R., eds., Backbone of the
855 Americas: Shallow subduction, plateau uplift, and ridge and terrane collision: Geological Society
856 of America Memoir 204, p. 31-65.
857 Ricketts, J.W., Kelley, S.A., Karlstrom, K.E., Schmandt, B., Donahue, M.S., and van Wijk, J., 2016,
858 Synchronous opening of the Rio Grande rift along its entire length at 25–10 Ma supported by
859 apatite (U-Th)/He and fission-track thermochronology, and evaluation of possible driving
860 mechanisms: Geological Society of America Bulletin, v. 128, p. 397-424.
861 Riggs, N.R., Reynolds, S.J., Lindner, P.J., Howell, E.R., Barth, A.P., Parker, W.G., and Walker, J.D.,
862 2013, The Early Mesozoic Cordilleran arc and Late Triassic paleotopography: The detrital record
863 in Upper Triassic sedimentary successions on and off the Colorado Plateau: Geosphere, v. 9, p.
864 602-613.

865 Saleeby, J., 2003, Segmentation of the Laramide slab—Evidence from the southern Sierra Nevada region:
866 Geological Society of America Bulletin, v. 115, p. 655-668.
867 Speed, R.C., and Sleep, N.H., 1982, Antler orogeny and foreland basin: A model: Geological Society of
868 America Bulletin, v. 93, p. 815-828.
869 Spencer, J.E., and Reynolds, S.J., 1990, Relationship between Mesozoic and Cenozoic tectonic features in
870 west central Arizona and adjacent southeastern California: Journal of Geophysical Research:
871 Solid Earth, v. 95, p. 539-555.
872 Spencer, J.E., Richard, S.M., Gehrels, G.E., Gleason, J.D., and Dickinson, W.R., 2011, Age and tectonic
873 setting of the Mesozoic McCoy Mountains Formation in western Arizona, USA: Geological
874 Society of America Bulletin, v. 123, p. 1258-1274.
875 Spencer, J.E., Richard, S.M., Reynolds, S.J., Miller, R.J., Shafiqullah, M., Gilbert, W.G., and Grubensky,
876 M.J., 1995, Spatial and temporal relationships between mid-Tertiary magmatism and extension in
877 southwestern Arizona: Journal of Geophysical Research: Solid Earth, v. 100, p. 10321-10351.
878 Spencer, J.E., Richard, S.M., Reynolds, S.J., Miller, R.J., Shafiqullah, M., Gilbert, W.G. and Grubensky,
879 M.J., 1995. Spatial and temporal relationships between mid-Tertiary magmatism and extension in
880 southwestern Arizona. Journal of Geophysical Research: Solid Earth, 100(B6), pp.10321-10351.
881 Stewart, J.H., 2005, Evidence for Mojave-Sonora megashear—Systematic left-lateral offset of
882 Neoproterozoic to Lower Jurassic strata and facies, western United States and northwestern
883 Mexico, in Anderson, T.H., Nourse, J.A., ,McKeee, J.W., Steiner, M.B., eds., The Mojave-Sonora
884 megashear hypothesis: Development, assessment, and alternatives: Geological Society of
885 America Special Paper 393, p. 209-231.
886 Trail, D., Bindeman, I.N., Watson, E.B., and Schmitt, A.K., 2009, Experimental calibration of oxygen
887 isotope fractionation between quartz and zircon: Geochimica et Cosmochimica Acta, v. 73, p.
888 7110-7126.
889 Valley, J.W., 2003, Oxygen isotopes in zircon, in Hanchar, J.M., and Hoskin, P.W.O., eds., Zircon:
890 Reviews in Mineralogy and Geochemistry, v. 53, p. 343-385.

891 Valley, J.W., and Kita, N.T., 2009, In situ oxygen isotope geochemistry by ion microprobe. Mineralogical
892 Association of Canada short course: secondary ion mass spectrometry in the earth sciences, v. 41,
893 p. 19-63.
894 Valley, J.W., Bindeman, I.N., and Peck, W.H., 2003, Empirical calibration of oxygen isotope
895 fractionation in zircon: Geochimica et Cosmochimica Acta, v. 67, p. 3257-3266.
896 Vervoort, J.D., Patchett, P.J., Blichert-Toft, J., and Albarède, F., 1999, Relationships between Lu–Hf and
897 Sm–Nd isotopic systems in the global sedimentary system: Earth and Planetary Science Letters,
898 v. 168, p. 79-99.
899 Walker, J.D., 1988. Permian and Triassic rocks of the Mojave Desert and their implications for timing
900 and mechanisms of continental truncation. Tectonics, 7(3), pp.685-709.
901 Wang X-L., Coble, M.A., Valley, J.W., Shu, X-J., Kitajima, K., Spicuzza, M.J., and Sun, T., 2014,
902 Influence of radiation damage on late Jurassic zircon from southern China: Evidence from in situ
903 measurement of oxygen isotopes, laser Raman, U-Pb ages, and trace elements: Chemical
904 Geology, v. 389, p. 122-136.
905 Wang, K., Plank, T., Walker, J.D., and Smith, E.I., 2002, A mantle melting profile across the Basin and
906 Range, SW USA: Journal of Geophysical Research: Solid Earth, v. 107.
907 Wells, M.L., Hoisch, T.D., Cruz-Uribe, A.M., and Vervoort, J.D., 2012, Geodynamics of synconvergent
908 extension and tectonic mode switching: Constraints from the Sevier-Laramide orogen: Tectonics,
909 p. 31., doi:10.1029/2011TC002913.
910 Whitmeyer, S.J., and Karlstrom, K.E., 2007, Tectonic model for the Proterozoic growth of North
911 America: Geosphere, v. 3, p. 220-259.
912 Wooden, J.L., Barth, A.P., and Mueller, P.A., 2013, Crustal growth and tectonic evolution of the Mojave
913 crustal province: Insights from hafnium isotope systematics in zircons: Lithosphere, v. 5, p. 17-
914 28.

Zhu, D.C., Zhao, Z.D., Niu, Y., Mo, X.X., Chung, S.L., Hou, Z.Q., Wang, L.Q., and Wu, F.Y., 2011, The Lhasa Terrane: Record of a microcontinent and its histories of drift and growth: Earth and Planetary Science Letters, v. 301, p. 241-255.

FIGURE CAPTIONS

Figure 1: Regional map of the southwestern U.S. Cordillera showing the boundaries (white dashed lines) and Nd model ages (in parentheses) of major crustal provinces (Dickinson and Lawton, 2001b; Whitmeyer and Karlstrom, 2007; Wooden et al., 2013). $^{87}Sr/^{86}Sr = 0.706$ position from Kistler (1990). SAF = San Andreas Fault. Sample location information is presented in Table 1.

Figure 2: Schematic tectonic maps and interpretive cross-sections of the southwestern U.S. Cordillera from the Late Jurassic to mid-Miocene. The heavy gray dashed line in maps and in cross-sections denotes the inferred edge of intact North American continental mantle lithosphere. Cross-sections are vertically aligned using the approximate reconstructed position of the Arizona-New Mexico border (~109 °E longitude). A) 150-100 Ma, subduction roll-back of the Farallon plate contributed to an extensional tectonic regime and opening of the Bisbee rift basin (Dickinson and Lawton, 2001a). The continental mantle lithosphere was the mantle source for Jurassic magmatism in western California and southern Arizona. B) 100-80 Ma; closure of the Arperos Basin and suturing of the Guerrero terrane (Martini et al., 2014) led to the development of a contractional tectonic regime including a retroarc thrust belt and foreland basin (Clinkscales and Lawton, 2015; Fitz-Diaz et al., 2017). The Sierra Nevada and Peninsular Ranges batholiths formed above the transition between asthenospheric upper mantle and continental mantle lithosphere (Coleman and Glazner, 1997). C) 80-40 Ma, the Laramide orogeny is associated with low-angle to flat-slab subduction, subduction erosion of the accretionary complex and forearc, underplating of the Pelona-Orocopia-Rand (POR) schist, arc migration toward the foreland, and increased contraction forming block uplifts and localized sedimentary basins (Coney and Reynolds, 1977;

941 Dickinson et al., 1988; Saleeby, 2003; Chapman, 2017). Most Laramide-age magmatism is interpreted to
942 have originated in the continental mantle lithosphere. By the end of the Laramide, the continental mantle
943 lithosphere in the Mojave region (west of ~114 °W longitude) had been at least partially removed. D) 40-
944 15 Ma, foundering or roll-back of the Farallon slab and subduction of the Pacific-Farallon spreading
945 center resulted in an extensional tectonic regime, metamorphic core-complex formation (Dickinson,
946 1991), and a rapid westward sweep of ignimbrite magmatism (Humphreys, 1995). The mantle source of
947 magmatism west of ~114 °W longitude was the depleted asthenospheric mantle or Farallon oceanic
948 lithosphere (Miller et al., 2000) and the mantle source east of ~114 °W longitude was the continental
949 mantle lithosphere (Farmer et al., 2008).
950
951 Figure 3: Plot of age vs. longitude for igneous rocks in the southern U.S. Cordillera showing the
952 eastward (100-40 Ma) and then westward (40-15 Ma) migration of magmatism (Table 1). A previous
953 compilation of igneous rock age data (shaded band) and estimate of the tectonic transition from a
954 contractional to extensional regime is adopted from Constenius et al. (2003). Squares are samples
955 analyzed in this study and shaded by mean zircon $\varepsilon Hf_{(t)}$ (Table 1).
956
957 Figure 4: Plot of mean zircon U-Pb age vs. A) mean zircon $\varepsilon Hf_{(t)}$, and C) mean $\delta^{18}O_{zrc}$ for samples
958 analyzed in this study (Table 1) and B) compiled age and whole rock $\varepsilon Nd_{(t)}$ of samples from the southern
959 U.S. Cordillera. εNd data are converted to equivalent εHf values using the terrestrial array (εHf
960 $=1.36\varepsilon Nd+2.95$) of Vervoort et al. (1999). There is a possible increase in zircon $\varepsilon Hf_{(t)}$ from 100 to 20
961 Ma, however, temporal isotopic trends are not clearly present. Compiled data are available in
962 Supplementary Table 4. Error bars for $\delta^{18}O_{zrc}$ data in panel C are sometimes smaller than the symbol.
963
964 Figure 5: A) Plot of individual (single-grain) zircon U-Pb age vs. zircon $\varepsilon Hf_{(t)}$ for samples that
965 contained inherited ages (e.g., premagmatic cores). Analyses are grouped by the lithospheric province
966 they were sampled from (Fig. 1). Mesozoic-Cenozoic and Proterozoic analyses from the same province
967 that plot along the same mean crustal evolution line suggest that the Mesozoic-Cenozoic igneous rocks

968 were derived from a lithospheric source with a similar age and composition to the lithospheric province
969 hosting the sample. Several analyses from the Mojave province do not fall along a common crustal
970 evolution line. B) An enlarged portion of panel A showing Mesozoic to Cenozoic analyses. Zircon $\varepsilon Hf_{(t)}$
971 data are available in Supplementary Table 2.
972
973 Figure 6: Plots of longitude (sub-parallel to orogenic structural grain) vs. A) mean zircon $\varepsilon Hf_{(t)}$ and
974 B) mean $\delta^{18}O_{zrc}$ from this study (Table 1). Uncertainties are 2σ for $\varepsilon Hf_{(t)}$ and 2 standard error (SE) for
975 $\delta^{18}O_{zrc}$. Samples are grouped according to whether their age is older or younger than 40 Ma, which is the
976 transition from a convergent to extensional tectonic regime at the end of the Laramide orogenic event
977 (Constenius et al., 2003). Compiled whole rock $\varepsilon Nd_{(t)}$ data in panel A is converted to equivalent εHf
978 values using the terrestrial array of Vervoort et al. (1999). Compiled $\delta^{18}O$ data in panel B come from
979 whole rock and minerals other than zircon and are converted to equivalent $\delta^{18}O_{zrc}$ (see text for details).
980 Compiled data are available in Supplementary Table 4. Error bars for $\delta^{18}O_{zrc}$ data are sometimes smaller
981 than the symbol.
982
983 Figure 7: A) Plot of longitude vs. lithospheric province model age (Nd or Hf) (solid line; Fig. 1)
984 and interpreted upper mantle source (dash-dot line). The upper mantle is interpreted to vary between a
985 predominately depleted mantle (DM) source and a continental mantle lithosphere (CML) source and the
986 (dash-dot) line for the interpreted mantle source is a proxy for the inferred geometry of the lithosphere-
987 asthenosphere boundary (LAB). The western extent of intact mantle lithosphere is estimated based on the
988 change in slope of the mantle limit lines in panel B. B) Plot of longitude vs. compiled whole rock $\varepsilon Nd_{(t)}$
989 of samples from the southwestern U.S. Cordillera, grouped by SiO_2 (wt. %). The isotopic composition of
990 the mantle source can be estimated by examining the most mafic samples and drawing a mantle limit line
991 (Miller et al., 2000; Chapman et al., 2017). Samples with ages of 15-110 Ma are shown to illustrate the
992 use of mantle limit lines. Changes in the inferred position of the LAB could be refined by using smaller
993 increments of time, as in Fig. 6. Compiled data are available in Supplementary Table 4.
994

995 Figure 8: Isotopic data from the central Mojave region (~115.5 to 117 °W longitude). Plot of age
996 vs. mean zircon $\varepsilon Hf_{(t)}$ and mean $\delta^{18}O_{zrc}$ for samples analyzed in this study (Table 1) and compiled whole
997 rock $\varepsilon Nd_{(t)}$ (converted to zircon $\varepsilon Hf_{(t)}$) and $\delta^{18}O$ data. Conversion of compiled data is the same as in Fig.
998 6 and is available in Supplementary Table 4. Increases in zircon $\varepsilon Hf_{(t)}$ and $\delta^{18}O_{zrc}$ during the Late
999 Cretaceous to early Miocene are attributed to partial removal and replacement of the continental mantle
1000 lithosphere with depleted asthenospheric mantle or oceanic lithosphere during the Laramide orogeny
1001 (Miller et al., 2000) and assimilation of underplated Pelona-Orocopia-Rand schist (Fig. 2) (Glazner and
1002 O'Neil, 1989). Temporal shifts to more juvenile zircon $\varepsilon Hf_{(t)}$ and mantle-like $\delta^{18}O_{zrc}$ values during the
1003 late Miocene to present are related to Basin and Range lithospheric extension and increasingly
1004 asthenospheric melt sources.

Figure 1

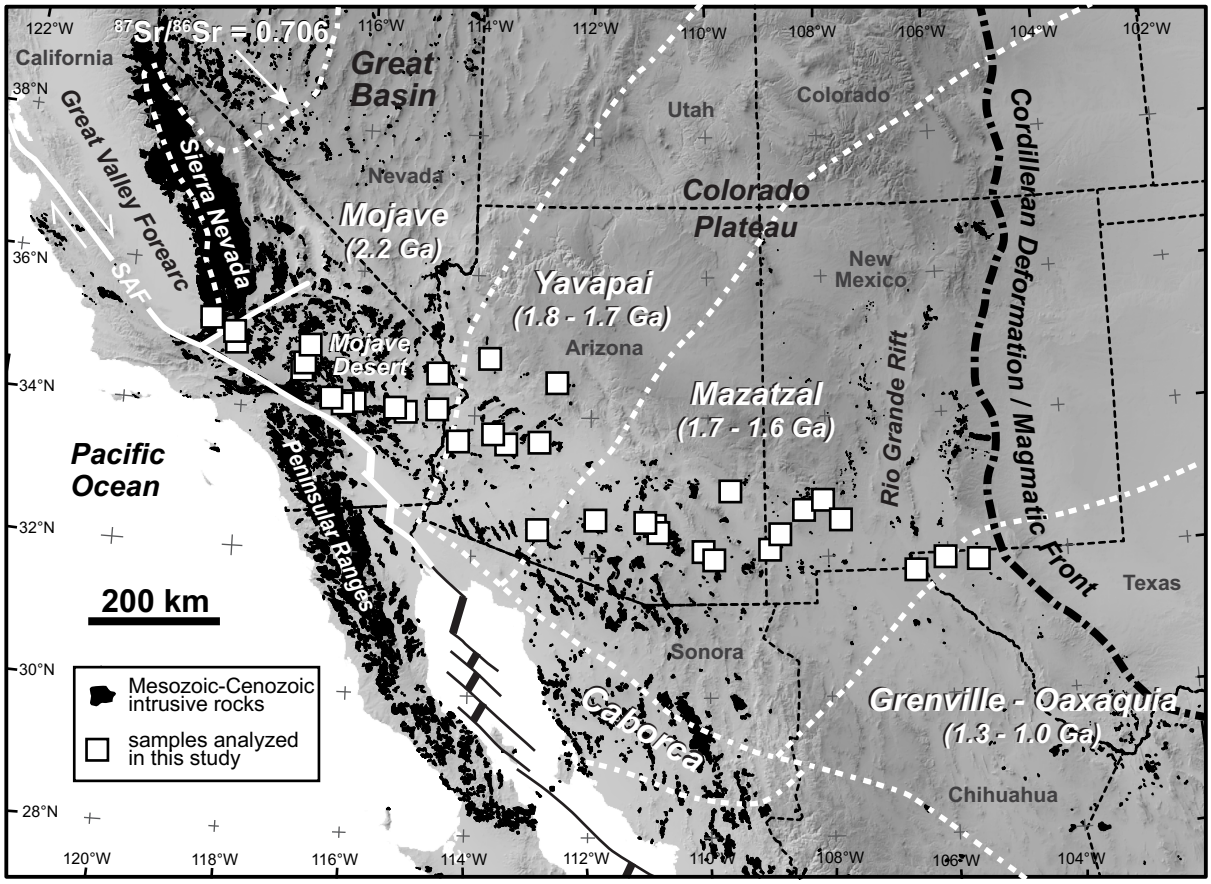
$^{87}Sr/^{86}Sr = 0.706$
Great Basin
Mojave (2.2 Ga)
Yavapai (1.8 - 1.7 Ga)
Mazatzal (1.7 - 1.6 Ga)
Colorado Plateau
Grenville - Oaxaquia (1.3 - 1.0 Ga)
Cabo rca
Pacific Ocean
Sierra Nevada
Great Valley Forearc
SAF
Peninsular Ranges
Mojave Desert
Rio Grande Rift
Cordilleran Deformation / Magmatic Front
California
Nevada
Utah
Colorado
New Mexico
Arizona
Texas
Sonora
Chihuahua
200 km
Mesozoic-Cenozoic intrusive rocks
samples analyzed in this study
122°W
120°W
118°W
116°W
114°W
112°W
110°W
108°W
106°W
104°W
102°W
38°N
36°N
34°N
32°N
30°N
28°N

Figure 2

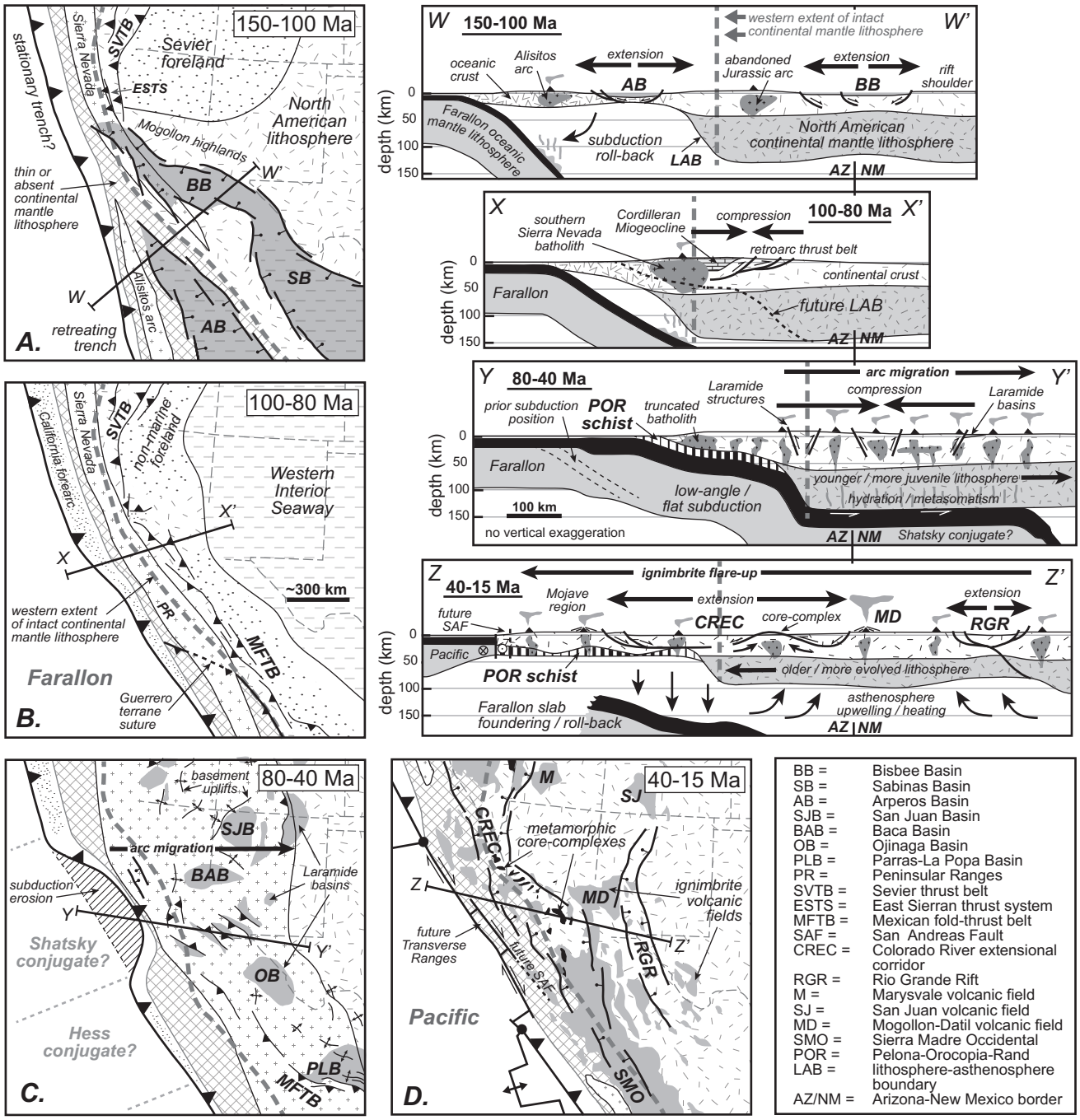
150-100 Ma
Sierra Nevada
SVTB
Sevier foreland
ESTS
North American lithosphere
Mogollon highlands
stationary trench?
thin or absent continental mantle lithosphere
BB
W'
W
SB
Alisitos arc
AB
retreating trench
A.
100-80 Ma
California forearc
non-marine foreland
Western Interior Seaway
X'
X
~300 km
western extent of intact continental mantle lithosphere
PR
MFTB
Farallon
Guerrero terrane suture
B.
W
150-100 Ma
western extent of intact continental mantle lithosphere
W'
oceanic crust
Alisitos arc
extension
AB
abandoned Jurassic arc
extension
BB
rift shoulder
depth (km)
0
50
100
150
Farallon oceanic mantle lithosphere
subduction roll-back
LAB
North American continental mantle lithosphere
AZ | NM
X
100-80 Ma
X'
southern Sierra Nevada batholith
Cordilleran Miogeocline
compression
retroarc thrust belt
continental crust
Farallon
future LAB
AZ | NM
Y
80-40 Ma
arc migration
Y'
prior subduction position
POR schist
truncated batholith
Laramide structures
compression
Laramide basins
Farallon
younger / more juvenile lithosphere
hydration / metasomatism
low-angle / flat subduction
100 km
no vertical exaggeration
AZ | NM
Shatsky conjugate?
Z
40-15 Ma
ignimbrite flare-up
Z'
Mojave region
extension
future SAF
CREC
core-complex
MD
extension
RGR
Pacific
older / more evolved lithosphere
POR schist
asthenosphere upwelling / heating
Farallon slab foundering / roll-back
AZ | NM
basement uplifts
80-40 Ma
SJB
arc migration
BAB
Laramide basins
subduction erosion
Y
Y'
Shatsky conjugate?
OB
Hess conjugate?
PLB
MFTB
C.
M
40-15 Ma
SJ
CREC
metamorphic core-complexes
Z
MD
ignimbrite volcanic fields
future Transverse Ranges
Z'
RGR
future SAF
Pacific
SMO
D.
BB = Bisbee Basin
SB = Sabinas Basin
AB = Arperos Basin
SJB = San Juan Basin
BAB = Baca Basin
OB = Ojinaga Basin
PLB = Parras-La Popa Basin
PR = Peninsular Ranges
SVTB = Sevier thrust belt
ESTS = East Sierran thrust system
MFTB = Mexican fold-thrust belt
SAF = San Andreas Fault
CREC = Colorado River extensional corridor
RGR = Rio Grande Rift
M = Marysvale volcanic field
SJ = San Juan volcanic field
MD = Mogollon-Datil volcanic field
SMO = Sierra Madre Occidental
POR = Pelona-Orocopia-Rand
LAB = lithosphere-asthenosphere boundary
AZ/NM = Arizona-New Mexico border

Figure 3

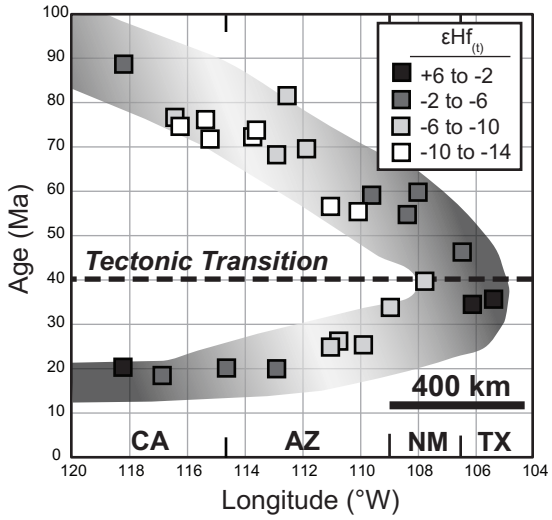
εHf(t)
+6 to -2
-2 to -6
-6 to -10
-10 to -14
Tectonic Transition
400 km
CA
AZ
NM
TX
Age (Ma)
Longitude (°W)
100
90
80
70
60
50
40
30
20
10
0
120
118
116
114
112
110
108
106
104

Figure 4

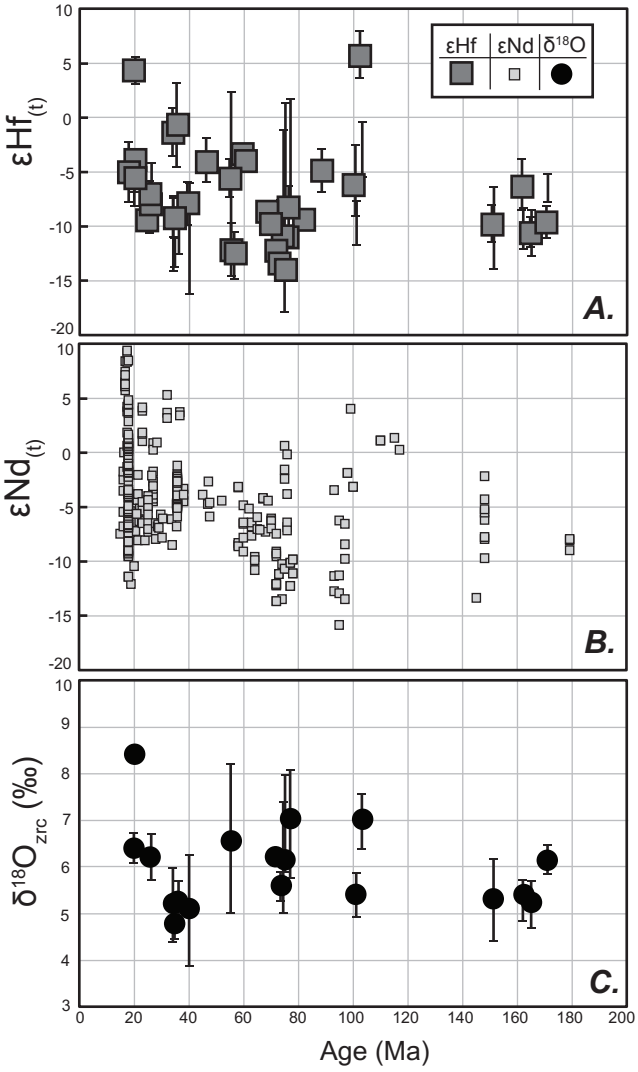

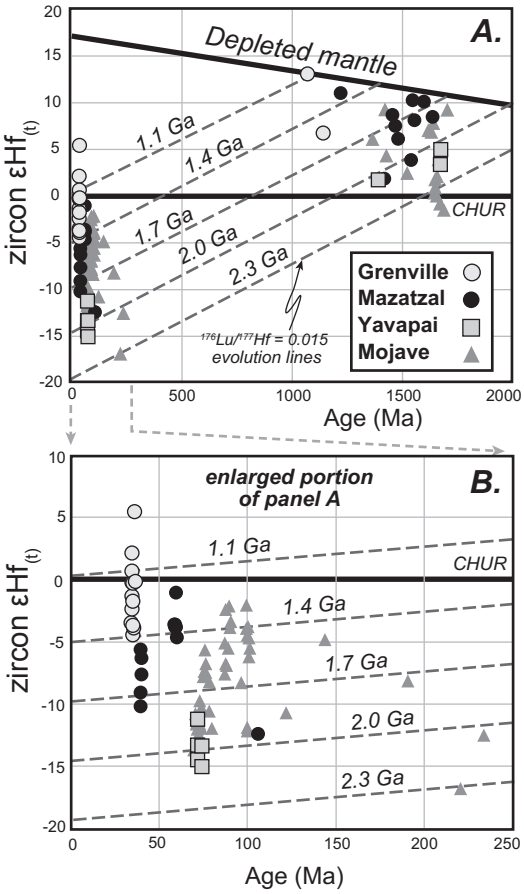
A.
Depleted mantle
1.1 Ga
1.4 Ga
1.7 Ga
2.0 Ga
2.3 Ga
CHUR
Grenville
Mazatzal
Yavapai
Mojave
176Lu/177Hf = 0.015
evolution lines
zircon εHf(t)
Age (Ma)
B.
enlarged portion
of panel A
1.1 Ga
CHUR
1.4 Ga
1.7 Ga
2.0 Ga
2.3 Ga
zircon εHf(t)
Age (Ma)

Figure 05

Figure 6

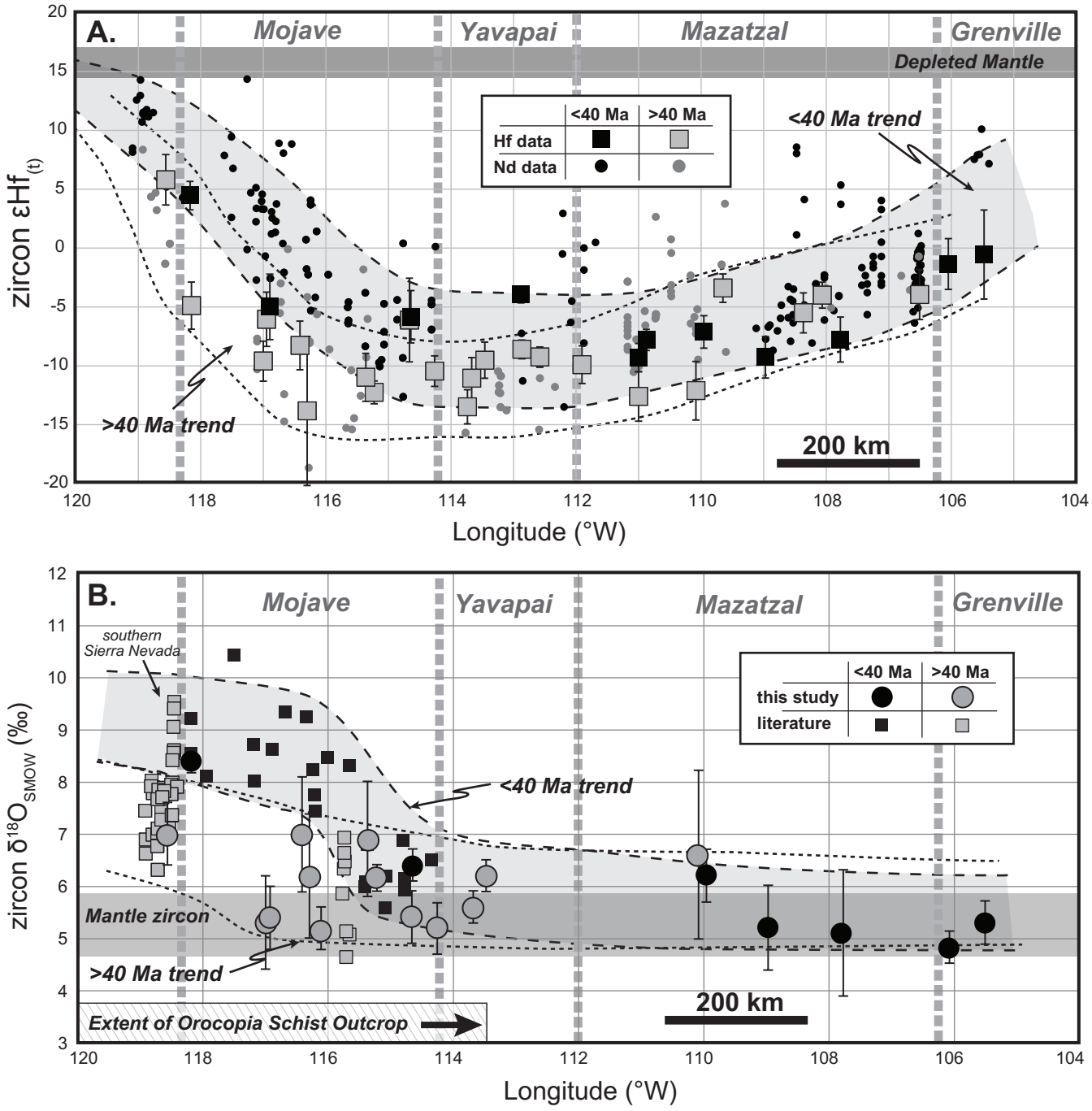
A.
Mojave
Yavapai
Mazatzal
Grenville
Depleted Mantle
<40 Ma
>40 Ma
Hf data
Nd data
<40 Ma trend
>40 Ma trend
200 km
zircon εHf(t)
Longitude (°W)
B.
Mojave
Yavapai
Mazatzal
Grenville
southern Sierra Nevada
this study
literature
<40 Ma trend
Mantle zircon
>40 Ma trend
Extent of Orocopia Schist Outcrop
200 km
zircon δ18OSMOW (‰)
Longitude (°W)

Figure 7

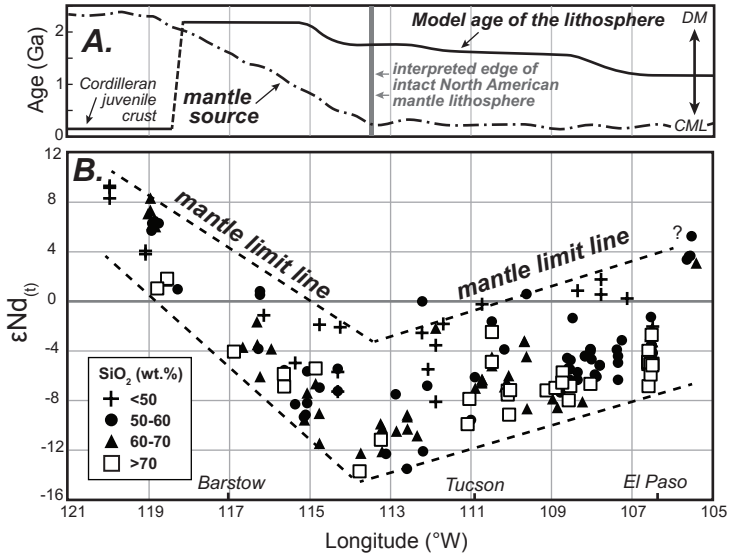
A.
Age (Ga)
Cordilleran juvenile crust
mantle source
Model age of the lithosphere
DM
interpreted edge of intact North American mantle lithosphere
CML
B.
εNd(t)
mantle limit line
mantle limit line
?
SiO2 (wt.%)
<50
50-60
60-70
>70
Barstow
Tucson
El Paso
Longitude (°W)

Figure 8

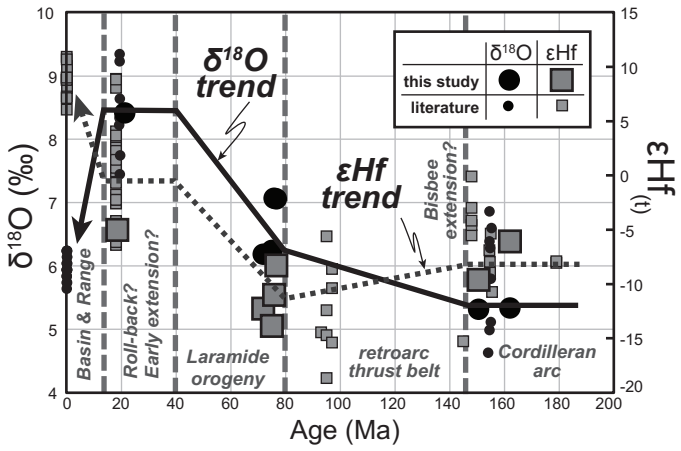
δ18O trend
εHf trend
δ18O
εHf
this study
literature
Basin & Range
Roll-back? Early extension?
Laramide orogeny
retroarc thrust belt
Bisbee extension?
Cordilleran arc
δ18O (‰)
εHf (t)
Age (Ma)